



# Onset of oxidative weathering of continents recorded in the geochemistry of ancient glacial diamictites



Richard M. Gaschnig <sup>a,\*</sup>, Roberta L. Rudnick <sup>a</sup>, William F. McDonough <sup>a</sup>, Alan J. Kaufman <sup>b</sup>, Zhaochu Hu <sup>c</sup>, Shan Gao <sup>c</sup>

<sup>a</sup> Geology Department, University of Maryland, College Park, MD 20742-4211, United States

<sup>b</sup> Geology Department and Earth System Science Interdisciplinary Center, University of Maryland, College Park, MD 20742-4211, United States

<sup>c</sup> State Key Laboratory for Geological Processes and Mineral Resources, China University of Geosciences, Wuhan, China

## ARTICLE INFO

### Article history:

Received 11 July 2014

Received in revised form 30 September 2014

Accepted 3 October 2014

Available online xxxx

Editor: B. Marty

### Keywords:

glaciation

oxygen

Precambrian

Great Oxidation Event

diamictite

upper continental crust

## ABSTRACT

Glacial diamictites deposited in the Mesoarchean, Paleoproterozoic, Neoproterozoic, and Paleozoic eras record temporal variations in their average compositions that reflect the changing composition of the upper continental crust (UCC). Twenty six of the 27 units studied show elevated chemical index of alternation (CIA) and low Sr abundances, regardless of their age, documenting pervasive weathering of the average UCC. Lower abundances of transition metals reflect a shift towards more felsic crustal compositions after the Archean. Superimposed on this chemical difference is the signal of the rise of oxidative weathering of the continents, recorded by changes in the absolute and relative abundances of the redox sensitive elements Mo and V. Neoproterozoic and Paleozoic diamictites show pervasive depletion in Mo and V, reflecting their loss from the continents due to increasing intensity of oxidative weathering, as also recorded in some of the Paleoproterozoic diamictites. A few of the Paleoproterozoic diamictites deposited after the Great Oxidation Event show no depletion in Mo and V (e.g., Gowganda), but such signatures could be inherited from their provenance. In contrast, the pre-GOE Duitschland diamictite (ca. 2.3–2.5 Ga) from South Africa reveals evidence of intense oxidative weathering (i.e., large depletions in Mo), supporting a growing body of observations showing the presence of measurable atmospheric oxygen prior to permanent loss of the mass independent fractionation signal in sulfur isotopes.

© 2014 Elsevier B.V. All rights reserved.

## 1. Introduction

The Earth is unique amongst all known planets in containing an atmosphere rich in free oxygen, which has been critical for the evolution and diversification of plants and animals. The historical record of fluctuations in atmospheric oxygen is therefore an area of central interest in the Earth sciences. Geological evidence documents that the Earth experienced significant rises in atmospheric oxygen levels in the early Paleoproterozoic (~2.4 to 2.2 Ga) and late Neoproterozoic (~0.7 to 0.55 Ga) eras (see Lyons et al., 2014, for a recent review). The former event is referred to as the Great Oxidation Event (GOE, Holland, 2006) and is identified in the sedimentary record by the disappearance of detrital uraninite, pyrite, and the mass independent fractionation (MIF) of sulfur isotopes and the first appearance of redbeds and a positive carbon isotope anomaly (e.g., Roscoe, 1973; Grandstaff, 1980; Farquhar et

al., 2000; Guo et al., 2009; Bekker and Kaufman, 2007), which are collectively believed to reflect the production of oxygen and its persistence of atmospheric oxygen levels above 2 ppmv (Pavlov and Kasting, 2002).

The trajectory of oxidation of the atmosphere following the GOE and prior to the Phanerozoic is largely derived from studies of redox sensitive metals and their isotopes, particularly in black shale deposits (Anbar et al., 2007; Asael et al., 2013; Gilleadeau and Kah, 2013; Kendall et al., 2013; Partin et al., 2013; Reinhard et al., 2009; Sahoo et al., 2012; Sekine et al., 2011; Siebert et al., 2005; Wille et al., 2007, 2013). Among these, Mo, Cr, and V are insoluble when reduced and soluble when oxidized (Calvert and Pedersen, 1993). The concentrations of these metals in fine-grained black shales reflect their changing budget in the oceans, which in turn reflects changing input from the continents. Oxidative weathering releases the oxidized, water soluble forms of these elements, which are later sequestered into carbon-rich muds in the reduced environments in which black shales accumulate. More direct evidence for oxidative weathering of continental rocks may be derived

\* Corresponding author.

E-mail address: gaschnig@umd.edu (R.M. Gaschnig).

from studying paleosols (Beukes et al., 2002; Crowe et al., 2013; Gay and Grandstaff, 1980; Grandstaff et al., 1986; Rye and Holland, 1998; Yang and Holland, 2003), whose mineralogy and behavior of redox-sensitive elements reflect prolonged interaction with the atmosphere.

In this study we open a new window into the history of sub-aerial oxidative weathering using the geochemistry of redox sensitive elements in glacial diamictites spanning ages from 2.9 to 0.3 Ga. These rocks are poorly-sorted lithified sediments derived from widespread physical erosion of the upper continental crust (UCC) by ice sheets and primarily deposited in marginal marine environments. Because these glacial deposits are geographically dispersed for a given time period, the systematic changes in the composition of the deposits can be used to track the changing composition of the UCC through time, including the rise of atmospheric oxygen and onset of oxidative weathering. We have analyzed major and trace elements in 125 diamictite samples from 27 formations in order to track the evolving composition of the UCC through time. Our data record systematic depletion of Mo and V in glacial deposits starting in the Paleoproterozoic, reflecting the loss of these elements from the continents due to increasing levels of oxidative weathering and hence increasing levels of free oxygen. Notably, the immediately pre-GOE ~2.3–2.5 Ga Duitschland diamictite shows evidence of intense oxidative weathering (large depletions in Mo), supporting a growing body of observations indicating the presence of intermittent, but significant atmospheric oxygen prior to permanent loss of the MIF signal in sulfur isotopes.

## 2. Samples

Glacial diamictites are poorly sorted sedimentary aggregates of material derived from the abrasion and erosion of soil and bedrock, followed by transport and deposition of the resulting sediments by melting glaciers and sea ice. While the term tillite is broadly synonymous for deposits on land, diamictite encompasses all such poorly-sorted deposits, whether deposited on land or in a shallow marine environment. Glacial diamictites typically consist of angular and rounded clasts of various sizes in a fine-grained matrix. Evidence of glacial origin include faceted and striated clasts of heterogeneous composition, and the presence of dropstones in otherwise fine-grained and finely-laminated intervals. The sediment that accumulates as glacial diamictite is typically derived from physically eroded bedrock with little evidence for chemical weathering (Nesbitt and Young, 1996) and diamictites derived from continental ice sheets have the potential to reflect an expansive provenance. For these reasons, V.M. Goldschmidt (1933) suggested that Pleistocene glacial sediments could provide a robust average composition of the UCC; a recent geochemical survey of valley tills from British Columbia lends credence to this approach (Canil and Lacourse, 2011).

Pre-Cenozoic glacial deposits occur in four broad geological intervals: Mesoarchean (ca. 2.9 Ga; Young et al., 1998), Paleoproterozoic (ca. 2.2 to 2.4 Ga; Bekker et al., 2001; Crowell, 1999; Melezhik et al., 2013), Neoproterozoic (ca. 0.75–0.58 Ga; Hoffman and Li, 2009), and Paleozoic (0.30 and 0.45 Ga; Hambrey, 1985; Visser, 1982). We have sampled glacial diamictites from all four of these intervals, spanning four modern continents; the individual stratigraphic units are listed in Table 1 with references for their ages and geological context. Individual sample locations are given in Table A1 and are plotted in Fig. A1. Samples consist primarily of massive diamictites and also include a few dropstone-bearing argillites. Samples of the Mesoarchean Coronation and Promise formations and Paleoproterozoic Timeball Hill, Duitschland, and Makganyene formations, and Ordovician Pakhuis Formation were obtained from drill cores, as were some of the Paleozoic Dwyka

Group samples. All other samples were taken from outcrops (Table 1).

Details pertaining to the early Paleoproterozoic ice ages are provided here because the GOE occurred during this interval. The Paleoproterozoic Huronian Supergroup in Canada contains three discrete glacial diamictites: the Ramsay Lake, Bruce, and Gowganda formations (in ascending stratigraphic order) (Melezhik et al., 2013; Young et al., 2001). The Pecors Formation, which contains dropstone-bearing argillites, directly overlies the Ramsay Lake diamictite and was also sampled here. Here, the loss of sulfur isotope MIF appears to occur between the Bruce and Ramsay Lake formations (Papineau et al., 2007). Correlative diamictites are also present in the Snowy Pass Group in the USA (Bekker et al., 2003; Houston et al., 1992), but of these, we have only sampled the Bottleg Creek Formation, and its absolute age and age relative to the sulfur MIF signal is unknown. In South Africa, Paleoproterozoic diamictites occur in two sub-basins of the Transvaal Supergroup. The Duitschland and Timeball Hill formations occur in the eastern Transvaal sub-basin where the disappearance of sulfur MIF is well documented between the two glacial deposits (Bekker et al., 2004; Guo et al., 2009). The Makganyene Formation occurs in the Griqualand West sub-basin, but its absolute age and position relative to the GOE and other Paleoproterozoic diamictites is unresolved (Moore et al., 2001; Coetze et al., 2006; Moore et al., 2012; Hoffman, 2013). The relationship between the eastern Transvaal and Huronian supergroups has recently been constrained by U-Pb zircon geochronology of volcanic ash beds (Rasmussen et al., 2013), which reveals that the Timeball Hill Formation represents the fourth and youngest glacial event in the Paleoproterozoic, occurring after the Gowganda Formation, whereas the Duitschland diamictite probably correlates with the Ramsay Lake Formation.

## 3. Methods

### 3.1. Sample preparation

Samples were crushed in a ceramic jaw crusher, and the resulting chips were handpicked to exclude clasts larger than 1 mm in diameter. Chips of diamictite matrix were then ground to a fine powder in a ceramic swing mill.

### 3.2. X-ray fluorescence analysis

Major element compositions used to calculate the chemical index of alteration in this paper were measured at Franklin and Marshall College. After determining loss on ignition, 0.4 g of anhydrous powder were mixed with 3.6 g of lithium tetraborate flux and fused in a platinum crucible. This fusion disc was then analyzed for major element abundances. Further details on the method and precision and accuracy are available at <http://www.fandm.edu/earth-and-environment/x-ray-laboratory>.

### 3.3. Total organic carbon analysis

For TOC measurements, ~5 g aliquots of powder were sequentially acidified with 3 M HCl for quantitative digestion of carbonate and repeatedly washed with H<sub>2</sub>O until solutions were pH neutral. Decalcified residues were dried overnight in an 80 °C oven, homogenized, and ~2–5 mg weighed into tin cups for organic carbon measurement with a Eurovector elemental analyzer. Abundances determined for residues were calculated from calibrations based on the carbon content of standard urea and normalized to whole rock values based on the percent carbonate determined through acidification.

**Table 1**  
Glacial diamictites investigated in this study.

Stratigraphic unit	Country (state/province)	Drill core or outcrop?	Number of samples	Number of sampled outcrops/cores	General reference	Depositional environmental	Max age (Ma)	Min age (Ma)	Age Ref.	Age relative to GOE
Mozaan Grp	S Africa	O	7	1	Young et al. (1998)	subaqueous	2980	2954	Mukasa et al. (2013)	Pre-GOE
Afrikander Frm*	S Africa	O	2	1	Guy et al. (2010)	subaqueous (?)	2981	2935	Armstrong et al. (1991); Kositcin and Krapez (2004)	Pre-GOE
Coronation Frm*	S Africa	DC	2	1	Guy et al. (2010)	subaqueous (?)	2981	2935	Armstrong et al. (1991); Kositcin and Krapez (2004)	Pre-GOE
Promise Frm*	S Africa	DC	2	1	Guy et al. (2010)	subaqueous (?)	2981	2935	Armstrong et al. (1991); Kositcin and Krapez (2004)	Pre-GOE
Duitschland Frm	S Africa	DC	5	2	Melezhik et al. (2013)	subaqueous	2480	2310	Rasmussen et al. (2013)	Pre-GOE
Timeball Hill Frm	S Africa	DC	6	1	Melezhik et al. (2013)	subaqueous	2256	2193	Rasmussen et al. (2013)	Post-GOE
Makganyene Frm	S Africa	DC	6	1	Melezhik et al. (2013)	subaqueous	2431	2222	Rasmussen et al. (2013)	unknown
Ramsay Lake Frm	Canada (Ontario)	O	5	2	Melezhik et al. (2013)	both	2450	2308	Rasmussen et al. (2013)	Pre-GOE
Pecors Frm	Canada (Ontario)	O	2	1	Melezhik et al. (2013)	subaqueous	2450	2308	Rasmussen et al. (2013)	Pre-GOE
Bruce Frm	Canada (Ontario)	O	3	1	Melezhik et al. (2013)	subaqueous	2450	2308	Rasmussen et al. (2013)	Post-GOE
Gowganda Frm	Canada (Ontario)	O	13	8	Melezhik et al. (2013)	subaqueous	2450	2308	Rasmussen et al. (2013)	Post-GOE
Bottle Creek Frm	USA (Wyoming)	O	4	1	Houston et al. (1992)	subaqueous (?)	2460	2090	Premo and Van Schmus, 1989	unknown
Pocatello Frm	USA (Idaho)	O	6	1	Keeley et al. (2013)	subaqueous	705	667	Keeley et al. (2013)	Post-GOE
Konnarock Frm	USA (Virginia)	O	8	3	Rankin (1993)	subaqueous	760	570	Rankin (1993)	Post-GOE
Gaskiers Frm	Canada (Newfoundland)	O	4	1	Carte and Eyles (2011)	subaqueous	581	580	Bowring et al. (2003)	Post-GOE
Nantuo Frm	China (Hubei)	O	13	6	Zhou et al. (2004)	subaqueous	655	635	Zhang et al. (2008)	Post-GOE
Gucheng Frm	China (Hubei)	O	5	5	Liu et al. (2008)	subaqueous	703	655	Liu et al. (2008)	Post-GOE
Blaubeker Frm	Namibia	O	3	1	Prave et al. (2011)	subaqueous	750	635	Prave et al. (2011)	Post-GOE
Kaigas Frm	Namibia	O	3	1	Frimmel (2011)	subaqueous	771	741	Frimmel (2011)	Post-GOE
Blasskranz	Namibia	O	1	1	Kaufman et al. (2009)	subaqueous	637	633	Kaufman et al. (2009)	Post-GOE
Chuos Frm	Namibia	O	1	1	Le Heron et al. (2013)	subaqueous	746	635	Hoffman (2011)	Post-GOE
Numees Frm	Namibia	O	4	2	Frimmel (2011)	subaqueous	741	555	Frimmel (2011)	Post-GOE
Ghaub Frm	Namibia	O	3	1	Hoffman (2011)	subaqueous	637	633	Hoffmann et al. (2004)	Post-GOE
Machareti Group	Bolivia	O	3	1	Starck and Papa (2006)	subaqueous	326	299	Starck and Papa (2006)	Post-GOE
Mandiyuti Group	Bolivia	O	3	1	Starck and Papa (2006)	subaqueous	326	299	Starck and Papa (2006)	Post-GOE
Pakhuis Frm	S Africa	DC	1	1	Young et al. (2004)	subaqueous	445	443	Sutcliffe et al. (2000)	Post-GOE
Dwyka Group	S Africa and Namibia	O & DC	10	6	Visser (1982)	subaqueous	312	288	Isbell et al. (2008)	Post-GOE

O = outcrop, DC = drill core.

\* The Afrikander, Coronation, and Promise Formations are components of the Witwatersrand Supergroup and are grouped as such in figures.

### 3.4. ICP-MS analysis

#### 3.4.1. Sample digestion

Most samples were digested for analysis by conventional high pressure HF/HNO<sub>3</sub> dissolution in Teflon Parr bombs, closely following the approach of Zhang et al. (2012a). Fifty milligrams of sample powder were dissolved in bombs with 3 mL HF + 1 mL HNO<sub>3</sub> for at least 5 days at ~180 °C. Solutions were then evaporated on a hot plate. Two mL of HNO<sub>3</sub> were added and evaporated, followed by the addition of 1 mL of HNO<sub>3</sub> and 2 mL of H<sub>2</sub>O. Bombs were then capped and returned to the oven for 12 h, after which sample solutions were transferred to centrifuge tubes and diluted to 15 mL with 2% HNO<sub>3</sub> containing a trace of HF.

A subset of samples was digested using the new NH<sub>4</sub>HF<sub>2</sub> method developed by Zhang et al. (2012b). For this approach ~0.2 g of purified NH<sub>4</sub>HF<sub>2</sub> was added to 50 mg of sample powder with a drop of water in a Teflon screw-top Savillex beaker. Beakers were placed in an oven for 12 h at ~230 °C. Upon return to room temperature, 2 mL of HNO<sub>3</sub> were added to the solid salt and the beakers were placed capped on the hot plate at 160 °C for at least an hour. Beakers were then uncapped and solutions were evaporated. Next, 1 mL of HNO<sub>3</sub>, 2 mL of H<sub>2</sub>O, and a trace of HF were added to the final salt and the beaker was capped and placed on the hot plate for at least 6 h.

#### 3.4.2. ICP-MS protocols

Most samples were analyzed for trace elements on a Thermo-Finnigan Element 2 high resolution-ICP-MS in the Department of Geology at the University of Maryland. Instrumental parameters are reported in Table A2. Samples were analyzed along with USGS whole-rock reference materials AGV-2, BHVO-1, GSP-1, and W-2 that were prepared at the same time as the samples. A constant amount of indium spike was added to each sample and used for drift correction. Elemental concentrations in samples were determined from calibration curves constructed from the four USGS standards. Overall precision and accuracy were evaluated by repeat analysis of separately dissolved AGV-2 aliquots treated as unknowns. These results, shown in Table A3, indicate that all elements are reproducible to better than 3% (based on % 1-sigma RSD of the mean), with the exceptions of V (6%), Mo (12%), and Sc (13%). Average values are within 10% of the working GEOREM values, with the exception of Pr, although the latter is only 2% outside the full published range of values.

Samples from the Konnarock, Nantuo, and Gucheng formations were analyzed on an Agilent 7700x quadrupole ICP-MS in the State Key Laboratory for Geological Processes and Mineral Resources at the China University of Geoscience in Wuhan, China. Instrumental parameters are reported in Table A2. Calibration was conducted using multi-element standard solutions as a basis and adjusting this calibration after analysis of dissolved whole-rock standards.

#### 3.4.3. Standard addition analyses

The concentration of Mo was determined in a subset of samples by standard addition, which provides a means of circumventing problems caused by differences between the matrices of the samples and standards, and by uncertainties in the Mo concentrations in the reference materials. Standard addition analyses consisted of analyzing four solutions per unknown sample. These consisted of: 1) a total analytical blank; 2) an unspiked aliquot of sample; 3) a spiked aliquot of sample; and 4) an aliquot of sample spiked with twice the volume of spike as the previous one. All aliquots were also spiked with an Rh standard solution, which was used for instrumental drift correction. Further description of standard addition analysis of Mo is provided in Gaschnig et al. (2014).

### 4. Data presentation

Major and selected trace elements are presented in Table 2. Also provided is the chemical index of alteration (CIA = molar Al<sub>2</sub>O<sub>3</sub>/(Al<sub>2</sub>O<sub>3</sub> + K<sub>2</sub>O + Na<sub>2</sub>O + CaO<sup>\*</sup>)), where CaO<sup>\*</sup> is corrected to remove the contribution of apatite and carbonate. The apatite correction was conducted by assigning all P<sub>2</sub>O<sub>5</sub> and a corresponding stoichiometric proportion of CaO to apatite. The carbonate correction was conducted following the approach of McLennan (1993), which assumes that the molar ratio of CaO to Na<sub>2</sub>O should be ≤1 in igneous systems and assigns excess CaO to carbonate after correcting for apatite.

Major element compositions of the diamictites vary widely within formations, and especially between formations of different age (Fig. 1). At least some of these variations reflect differences in the regional geology of the surfaces traversed by the glaciers. In addition, CIA values of the diamictites are generally higher than those of fresh igneous rocks (Fig. 2: Young and Nesbitt, 1982), demonstrating that most samples record a history of weathering.

The rise of oxidative weathering is best documented by the behavior of multivalent elements whose solubility changes as a function of the oxidation state of the system. For this purpose, we focus on the behavior of Mo, Cr, and V. All three of these elements are more soluble in their oxidized forms (6+ for Mo and Cr, 5+ for V) relative to their reduced forms (4+ for Mo and V, 3+ for Cr). To quantify the magnitude of depletion or enrichment of these elements, we plot them relative to elements that have typically a single oxidation state and show similar partitioning behavior during mantle melting. Molybdenum's partitioning behavior is comparable to those of the light rare earth elements (LREE, all 3+), so it is plotted between Pr and Ce on a multi-element plot (Newsom and Palme, 1984) (Fig. 3). Strontium (2+), which is highly soluble and can be used as a monitor of subaerial weathering, has similar partitioning behavior during mantle melting and is plotted between Pr and Nd (Fig. 3). Multivalent, moderately compatible transition metals, V and Cr, are plotted after the heavy rare earth elements (HREE) alongside similar metals with a single oxidation state (Fig. 4). Data are normalized to the UCC compositional model of Rudnick and Gao (2003), with all elements additionally normalized to the average UCC concentration of Y in Figs. 3 and 4 (and Al<sub>2</sub>O<sub>3</sub> in Fig. 8), in order to remove the effects of quartz and/or carbonate dilution.

Fig. 3 shows that nearly all of the Neoproterozoic and Paleozoic samples are depleted in Mo relative to neighboring REE, in some cases by as much as an order of magnitude. In contrast, most Paleoproterozoic samples from Wyoming, Ontario, and the western Transvaal sub-basin in South Africa (Makganyene Formation), and the Mesoarchean samples have Mo abundances similar to the LREEs, or are more enriched. However, Paleoproterozoic samples from the Timeball Hill and Duitschland formations in South Africa are generally depleted in Mo relative to the LREEs. Nearly all samples, regardless of age, are depleted in Sr, sometimes by more than an order of magnitude (Fig. 3). Exceptions are two carbonate-bearing Neoproterozoic diamictites from Namibia, which are enriched in Sr, and the Paleoproterozoic Wyoming samples that show no significant Sr depletions.

Fig. 4 shows the double normalized log-normal mean concentrations of HREE and first row transition metals for each locality. Means are plotted here because the intra-locality variability is generally small for these elements. The exceptions to this are the Paleozoic Dwyka Group of South Africa, and the Paleoproterozoic localities from South Africa, which, for this reason, are plotted separately. Like Mo, age-dependent variations exist in the relative abundances of the first row transition metals, with Neoproterozoic and younger localities generally being depleted in transition metals relative to the HREE and the UCC, and Paleoproterozoic and

**Table 2**

Sample	Strat unit	SiO <sub>2</sub> XRF <sup>a</sup>	TiO <sub>2</sub>	Al <sub>2</sub> O <sub>3</sub>	Fe <sub>2</sub> O <sub>3</sub> T	MnO	MgO	CaO	Na <sub>2</sub> O	K <sub>2</sub> O	P <sub>2</sub> O <sub>5</sub>	LOI <sup>b</sup>	CIA <sup>c</sup>	TOC <sup>d</sup>	Mg# <sup>e</sup>	Sc ICP-MS	V	Cr	Co	Ni	Sr	Y	Mo <sup>f</sup>	La	Ce	Pr	Nd	Sm	Eu	Gd	Tm	Yb	Lu	V/V <sup>a,g</sup>	Cr/Cr <sup>a,g</sup>	Mo/Mo <sup>a,g</sup>	Sr/Sr <sup>a,g</sup>	
<b>Mesoarchean</b>																																						
<b>South Africa</b>																																						
13RMG005	Mozaan Grp	58.84	0.39	8.95	23.41	0.11	2.89	0.38	0.78	1.67	0.07	2.51	71	0.20	10.3	72.8	357	18.9	132	46.9	10.9	1.6	13.6	26.9	3.17	11.7	2.22	0.559	2.04	0.179	1.17	0.175	1.156	4.310	3.350	0.341		
13RMG006	Mozaan Grp	58.13	0.37	8.75	24.44	0.13	3.02	0.52	0.63	1.42	0.05	2.54	72	0.06	20	10.5	78.0	350	19.6	129	64.1	11.7	1.42	14.3	27.3	3.24	12.2	2.29	0.593	2.12	0.180	1.17	0.174	1.228	4.110	2.847	0.452	
13RMG007	Mozaan Grp	58.86	0.38	8.94	23.59	0.16	3.24	0.13	0.08	0.96	0.06	3.62	88	0.07	21	10.0	77.3	365	20.6	123	18.5	11.5	1.0	14.3	28.9	3.38	12.8	2.43	0.626	2.25	0.184	1.22	0.186	1.207	4.280	1.899	0.124	
13RMG008	Mozaan Grp	59.31	0.41	9.07	23.01	0.15	2.90	0.14	0.72	1.78	0.06	2.46	74	0.05	20	7.81	75.7	394	20.6	132	45.3	12.0	0.81	15.5	30.3	3.60	13.3	2.51	0.618	2.23	0.193	1.22	0.190	1.324	5.247	1.456	0.290	
13RMG009	Mozaan Grp	53.99	0.41	9.52	26.42	0.13	3.30	0.76	0.66	1.51	0.06	3.25	72	0.07	20	11.3	78.2	371	23.2	183	97.8	11.6	1.0	15.0	29.5	3.53	13.1	2.51	0.627	2.30	0.186	1.19	0.183	1.162	3.866	1.858	0.642	
13RMG010	Mozaan Grp	57.64	0.36	8.51	23.21	0.13	2.89	1.25	0.56	1.69	0.06	3.70	70	0.04	20	9.45	71.6	356	19.0	154	10.5	0.97	13.5	26.7	3.13	11.7	2.25	0.584	2.00	0.168	1.08	0.164	1.228	4.484	2.006	1.122		
13RMG011	Mozaan Grp	55.92	0.33	7.82	28.54	0.11	2.99	0.16	0.51	0.80	0.05	2.78	81	0.05	17	9.29	64.3	250	15.1	107	36.4	9.70	0.77	12.7	24.0	2.90	10.3	2.01	0.498	1.65	0.143	0.923	1.039	1.209	3.550	1.734	0.299	
13RMG001	Afrikander Frm	63.97	0.24	8.49	8.37	0.13	9.31	5.94	0.50	0.41	0.04	2.61	80	0.04	69	21.3	115	954	38.1	201	135	9.93	0.31	7.33	14.1	1.58	6.36	1.30	0.410	1.43	0.167	1.06	0.166	1.300	5.648	1.242	1.831	
13RMG003	Afrikander Frm	63.86	0.26	8.32	8.62	0.14	9.37	5.99	0.52	0.34	0.04	2.65	83	0.04	68	22.3	109	988	41.8	197	149	9.70	0.12	7.34	14.7	1.67	6.68	1.36	0.413	1.42	0.163	1.03	0.162	1.227	5.462	0.465	1.932	
BAB1-4031	Promise Frm	61.01	0.66	15.48	11.59	0.11	3.90	0.54	0.54	2.43	0.06	3.68	78	0.07	40	17.1	116	612	36.0	244	26.5	17.7	0.85	27.8	54.9	5.98	23.0	4.22	1.47	3.55	0.273	1.76	0.260	1.178	4.160	0.880	0.096	
BAB1-4042	Promise Frm	85.64	0.09	5.18	1.23	0.02	0.40	1.25	0.93	1.48	0.02	1.76	60	0.04	39	1.06	9.6	24.2	2.12	10.6	84.4	2.71	0.10	4.32	8.24	0.888	3.38	0.63	0.248	0.56	0.044	0.282	0.045	0.937	2.713	0.676	2.060	
BAB1-3171	Coronation Frm	72.33	0.47	15.08	3.34	0.04	1.84	0.46	0.33	3.00	0.07	3.04	78	0.06	52	10.9	77.4	279	17.5	89.0	15.4	1.0	32.9	66.7	7.25	27.4	4.86	1.14	3.58	0.230	1.50	0.233	1.038	3.423	0.864	0.244		
BAB1-3216	Coronation Frm	72.15	0.52	15.67	3.94	0.06	1.95	0.70	0.30	2.57	0.06	2.07	81	0.06	49	8.41	83.6	286	21.4	103	75.0	13.6	1.1	28.8	56.0	6.19	23.5	4.18	1.02	3.21	0.219	1.46	0.223	1.303	3.591	1.101	0.267	
<b>Paleoproterozoic</b>																																						
<b>Wyoming</b>																																						
12RMG032	Bottle Creek Frm	72.19	0.46	13.12	3.90	0.05	2.19	0.61	4.39	1.82	0.11	1.15	57	0.07	53	8.47	77.5	95.5	11.3	33.8	170	11.9	0.42	18.0	43.5	4.22	15.9	2.96	0.842	2.49	0.196	1.31	0.202	1.263	1.648	0.582	0.834	
12RMG033	Bottle Creek Frm	70.62	0.47	13.42	4.50	0.05	2.70	0.49	3.92	2.00	0.12	1.71	59	0.06	54	8.25	76.7	92.2	12.8	41.5	138	11.2	0.73	14.4	22.5	3.61	13.7	2.52	0.621	2.07	0.189	1.24	0.195	1.291	1.514	1.526	1.013	
12RMG034	Bottle Creek Frm	71.66	0.48	13.18	4.08	0.05	2.43	0.52	3.97	1.89	0.12	1.62	59	0.08	54	8.08	75.5	102	13.2	37.8	142	7.47	0.41	8.57	14.7	2.14	8.27	1.61	0.473	1.40	0.150	1.02	0.160	1.417	1.660	1.384	1.666	
12RMG035	Bottle Creek Frm	70.90	0.46	13.49	4.31	0.03	2.45	0.46	4.10	1.76	0.12	1.92	59	0.17	53	9.17	75.8	105	10.7	39.3	111	8.56	0.53	12.3	28.3	3.52	13.2	2.54	0.665	1.93	0.173	1.12	0.170	1.294	1.787	1.001	0.738	
<b>Ontario</b>																																						
12RMG036	Ramsay Lake Frm	82.09	0.26	7.91	2.84	0.06	0.98	1.29	1.86	1.60	0.05	1.07	53	0.05	41	5.37	37.5	38.7	9.57	24.3	203	8.72	0.83	28.8	53.0	5.53	19.0	3.07	0.615	2.44	0.122	0.765	0.122	0.988	0.910	0.910	0.822	
12RMG037	Ramsay Lake Frm	77.60	0.38	10.81	3.01	0.05	2.23	0.15	0.16	4.06	0.07	1.48	69	0.09	59	5.45	65.1	98.9	18.6	51.2	156	12.0	2.2	27.4	58.8	6.42	23.2	4.09	0.765	3.13	0.197	1.23	0.172	1.436	1.656	2.147	0.054	
12RMG040	Gowganda Frm	69.30	0.47	13.83	5.84	0.03	2.17	0.34	0.58	1.40	0.11	1.43	57	0.04	52	7.58	67.5	76.5	14.1	35.9	135	11.6	1.7	33.7	59.1	6.46	22.5	3.54	0.768	2.31	0.180	1.23	0.181	1.229	1.103	1.635	0.270	
12RMG041	Gowganda Frm	70.49	0.44	13.77	4.77	0.06	2.21	0.26	4.13	2.08	0.08	1.59	59	0.08	48	2.44	81.8	48.2	67.3	94.7	147	12.4	3.04	24.5	55.8	21.2	3.04	0.759	2.44	0.196	0.765	0.193	2.509	2.493	1.554	0.283		
12RMG042	Gowganda Frm	71.27	0.41	14.12	2.87	0.02	2.19	0.35	4.23	2.90	0.10	1.54	57	0.07	60	6.03	85.6	54.5	7.20	13.8	90.3	13.4	0.82	27.2	49.5	49.5	6.02	21.8	4.03	0.982	2.98	0.196	1.35	0.207	1.636	1.395	0.941	0.354
12RMG043	Gowganda Frm	62.28	0.61	17.37	5.16	0.04	3.81	0.41	3.60	3.84	0.12	2.76	62	0.09	59	15.7	151	145	7.20	46.6	87.5	21.9	1.3	25.6	50.4	6.22	22.8	4.61	1.14	3.86	3.43	2.26	3.69	2.304	1.417	0.333		
12RMG044	Gowganda Frm	70.47	0.40	12.96	5.02	0.03	2.86	0.27	4.64	1.66	0.11	0.20	59	0.04	45	8.76	70.9	79.6	10.2	19.2	73.1	13.8	1.3	23.2	39.3	5.21	19.3	3.39	0.753	2.85	0.124	0.885	1.41	1.618	1.313	5.412	0.346	
12RMG055	Gowganda Frm	66.70	0.54	14.16	6.93	0.05	2.86	0.27	4.64	1.66	0.11	0.20	59	0.06	45	13.0	108	126	8.4	20.9	40.9	10.4	2.6	30.7	58.1	5.81	20.7	3.54	0.753	2.41	0.124	0.885	1.41	1.618	1.313	5.412	0.346	
12RMG057	Gowganda Frm	65.88	0.67	15.24	5.62	0.11</td																																

**Table 2 (continued)**

Sample	Strat unit	SiO <sub>2</sub> XRF <sup>a</sup>	TiO <sub>2</sub>	Al <sub>2</sub> O <sub>3</sub>	Fe <sub>2</sub> O <sub>3</sub> T	MnO	MgO	CaO	Na <sub>2</sub> O	K <sub>2</sub> O	P <sub>2</sub> O <sub>5</sub>	LOI <sup>b</sup>	CIA <sup>c</sup>	TOC <sup>d</sup>	Mg# <sup>e</sup>	Sc ICP-MS	V	Cr	Co	Ni	Sr	Y	Mo <sup>f</sup>	La	Ce	Pr	Nd	Sm	Eu	Gd	Tm	Yb	Lu	V/V <sup>g</sup>	Cr/Cr <sup>g</sup>	Mo/Mo <sup>h</sup>	Sr/Sr <sup>h</sup>	
<b>China</b>																																						
GCH01	Gucheng Fmn	66.51	0.62	14.42	5.37	0.16	2.20	1.37	1.24	3.55	0.12	4.43	65	45	13.0	68.3	56.9	13.6	30.0	53.1	34.8	0.19	35.3	64.1	8.21	32.1	6.61	1.49	6.19	0.508	3.05	0.467	0.592	0.723	0.159	0.151		
GCH02	Gucheng Fmn	65.57	0.61	14.06	5.54	0.28	2.20	2.11	1.37	3.17	0.12	4.95	64	0.10	44	12.9	75.1	53.0	12.8	28.4	64.4	29.7	0.25	31.8	63.8	7.64	29.1	5.95	1.14	5.34	0.490	3.03	0.461	0.658	0.696	0.215	0.193	
GCH03	Gucheng Fmn	67.94	0.62	14.12	5.32	0.22	2.14	0.98	1.25	3.22	0.12	4.01	67	0.15	44	12.9	75.1	55.5	13.3	28.7	46.7	31.7	0.26	34.7	66.9	8.12	31.4	6.39	1.51	5.75	0.499	3.02	0.471	0.650	0.715	0.209	0.131	
GCH05	Gucheng Fmn	66.18	0.67	14.97	5.71	0.48	2.19	0.47	0.63	3.63	0.14	4.92	73	43	14.4	78.9	62.4	15.1	32.4	33.1	34.1	0.28	47.3	81.0	9.64	36.0	6.84	1.27	6.05	0.508	3.03	0.479	0.641	0.713	0.191	0.079		
GCH06	Gucheng Fmn	67.91	0.62	13.68	4.37	2.08	1.48	0.42	0.58	3.36	0.16	5.34	73	40	12.5	69.4	55.8	11.4	69.8	43.5	44.9	0.83	41.2	76.4	9.71	38.3	8.16	1.76	7.91	0.608	3.50	0.532	0.574	0.790	0.073	0.104		
NT02	Nantuo Fmn	66.69	0.63	14.83	5.68	0.18	2.27	1.08	1.31	3.53	0.12	3.66	66	0.13	44	13.0	73.7	50.9	11.7	27.0	64.7	28.7	0.27	33.9	65.5	7.71	29.7	5.93	1.28	5.47	0.472	2.98	0.463	0.642	0.697	0.224	0.189	
NT03	Nantuo Fmn	65.97	0.62	14.70	5.36	0.14	2.16	1.39	1.25	3.62	0.12	4.66	65	0.11	44	13.2	75.5	65.6	12.4	30.0	72.5	30.8	0.17	35.0	66.0	8.09	30.9	6.21	1.34	5.65	0.491	3.04	0.464	0.650	0.863	0.141	0.207	
NT04	Nantuo Fmn	67.33	0.63	14.53	4.17	0.10	1.66	1.57	1.19	3.76	0.12	4.92	65	44	12.9	75.2	59.5	13.1	27.3	107	28.4	0.22	35.6	69.4	8.32	31.6	6.26	1.31	5.45	0.483	3.04	0.470	0.653	0.774	0.169	0.293		
NT05	Nantuo Fmn	58.73	0.71	16.29	6.82	0.24	3.71	2.31	2.27	3.10	0.17	5.66	60	52	16.1	98.0	58.3	20.0	37.5	87.7	33.2	0.38	24.5	53.1	6.64	26.3	5.94	1.15	5.40	0.536	3.24	0.497	0.737	0.547	0.302	0.302		
NT05-2A	Nantuo Fmn	64.56	0.62	13.77	5.40	0.09	2.40	2.61	0.97	3.29	0.12	6.18	68	0.04	47	13.2	62.1	54.6	19.5	50.2	82.9	28.2	0.20	29.1	56.7	6.67	4.49	24.9	5.15	1.14	4.49	0.427	2.83	0.436	0.552	0.574	0.190	0.285
NT05-2B	Nantuo Fmn	66.13	0.59	13.22	6.38	0.09	2.52	1.78	0.96	2.94	0.12	5.25	68	44	10.7	71.1	47.3	10.5	23.2	73.4	29.1	0.19	36.5	71.1	8.15	29.5	5.75	1.32	4.88	0.446	2.90	0.441	0.697	0.750	0.151	0.206		
NT05-2C	Nantuo Fmn	66.19	0.61	13.42	5.85	0.08	2.60	1.78	0.81	3.12	0.11	5.41	69	47	12.4	86.3	85.6	6.83	23.0	53.3	27.9	0.16	34.2	66.9	7.72	28.3	5.63	1.11	4.77	0.426	2.79	0.429	0.799	1.570	0.133	0.158		
NT05-2D	Nantuo Fmn	66.60	0.62	13.84	4.82	0.08	2.45	1.68	0.85	3.38	0.12	5.55	69	50	13.6	89.4	56.9	8.76	24.8	56.9	29.0	0.24	34.7	68.3	7.98	29.1	5.75	1.15	4.87	0.443	2.90	0.435	0.784	0.879	0.194	0.162		
NT06	Nantuo Fmn	64.54	0.64	14.58	5.31	0.12	2.21	2.00	1.67	3.32	0.12	5.50	62	45	13.4	73.8	59.9	12.2	31.5	101	32.5	0.43	34.5	69.5	8.14	30.9	6.17	1.32	5.64	0.506	3.28	0.492	0.613	0.787	0.342	0.281		
NT08	Nantuo Fmn	65.10	0.63	14.62	5.30	0.13	2.16	2.18	1.44	3.43	0.12	4.89	64	0.05	45	12.3	72.8	68.1	13.4	34.3	69.1	31.2	0.28	34.9	70.6	8.29	31.9	6.35	1.38	5.75	0.499	3.19	0.484	0.638	0.894	0.216	0.188	
7201	Nantuo Fmn	64.95	0.63	14.16	5.16	0.09	2.45	1.97	0.99	3.63	0.13	5.69	67	48	13.2	77.0	63.3	16.4	32.0	60.8	29.5	0.22	34.4	68.3	8.03	30.2	6.16	1.25	5.43	0.490	2.94	0.453	0.670	0.723	0.179	0.173		
7202	Nantuo Fmn	63.82	0.62	14.44	5.14	0.11	2.42	2.40	0.81	3.80	0.13	6.32	69	48	13.4	77.7	66.5	13.9	33.4	57.6	29.8	0.24	37.0	71.9	8.36	31.4	6.38	1.32	5.56	0.484	2.97	0.466	0.663	0.822	0.186	0.156		
7203	Nantuo Fmn	64.90	0.62	14.18	4.43	0.07	2.21	2.46	0.80	3.76	0.12	6.45	68	50	13.2	77.8	63.2	12.5	28.4	71.2	29.0	0.23	36.3	71.7	8.29	30.8	6.22	1.51	5.54	0.481	2.90	0.460	0.674	0.832	0.178	0.195		
<b>Idaho</b>																																						
12RMG016	Pocatello Fmn	71.05	0.94	11.81	5.43	0.03	0.92	1.71	0.31	3.89	0.23	3.68	71	0.07	25	8.41	69.1	46.2	12.6	23.6	184	47.7	0.22	87.4	173	18.9	68.8	12.0	2.25	10.0	0.690	4.31	0.363	0.638	0.757	0.073	0.218	
12RMG017	Pocatello Fmn	70.71	0.90	12.67	6.16	0.07	1.59	0.49	0.73	3.95	0.20	2.53	68	0.06	34	10.0	74.9	61.9	12.0	29.6	45.6	40.4	0.29	67.8	133	15.2	55.8	9.87	1.87	8.25	0.606	3.82	0.574	0.666	0.953	0.122	0.068	
12RMG018	Pocatello Fmn	72.59	0.83	11.64	5.59	0.05	1.40	0.76	0.88	3.48	0.18	2.59	65	0.05	33	8.81	68.9	53.1	11.8	26.8	61.1	47.6	0.23	71.0	141	15.9	58.5	10.3	2.03	9.2	0.660	4.01	0.590	0.645	0.878	0.093	0.087	
12RMG019	Pocatello Fmn	72.43	0.81	11.94	5.71	0.07	1.56	0.46	1.07	3.43	0.18	2.34	67	0.06	35	8.99	68.2	53.0	12.4	27.0	44.1	35.9	0.27	76.6	152	16.9	61.7	10.6	1.97	8.5	0.541	3.39	0.518	0.674	0.845	0.101	0.059	
12RMG022	Pocatello Fmn	63.78	1.80	14.79	7.36	0.10	2.01	0.74	1.48	4.30	0.17	3.19	67	0.08	35	13.3	126	82.5	20.8	30.3	128	56.7	3.1	115	229	26.7	69.0	16.0	3.43	12.4	0.758	4.77	0.698	0.882	0.837	0.172	0.112	
12RMG023	Pocatello Fmn	66.02	1.58	13.36	7.47	0.10	2.04	0.62	1.43	3.89	0.38	3.11	66	0.09	35	10.7	94.4	17.3	31.1	97.2	41.4	1.8	81.9	171	19.4	70.5	11.8	2.51	8.9	0.561	3.56	0.524	0.626	0.862	0.170	0.114		
<b>Namibia</b>																																						
13RMG020	Blaubeker Fmn	76.93	0.54	10.05	3.95	0.03	1.51	0.32	1.52	3.02	0.14	1.99	62	0.05	43	8.14	67.9	42.2	4.00	13.6	55.4	28.8	0.32	30.6	59.7	7.34	27.7	5.70	1.17	5.02	0.430	2.67	0.398	0.804	1.245	0.283	0.176	
13RMG022	Blaubeker Fmn	75.03	0.47	9.85	4.27	0.05	1.36	1.42	2.13	2.83	0.11	2.48	53	0.05	39	4.85	51.5	34.7	3.45	10.3	91.5	21.2	0.25	29.1	54.0	6.08	20.7	3.92	0.862	3.49	0.339	2.20	0.331	0.868	1.429	0.264	0.352	
13RMG025	Blaubeker Fmn	77.47	0.55	10.26	2.54	0.09	1.33	0.33	1.47	3.39	0.12	2.46	62	0.07	51	7.90	94.5	49.8	8.49	15.7	47.2	26.3	0.42	27.5	54.4	6.23	26.1	5.21	1.10	4.63	0.400	2.52	0.389	0.810	1.026	0.161	0.245	
13RMG029	Kaigas Fmn	62.22	0.98	1																																		

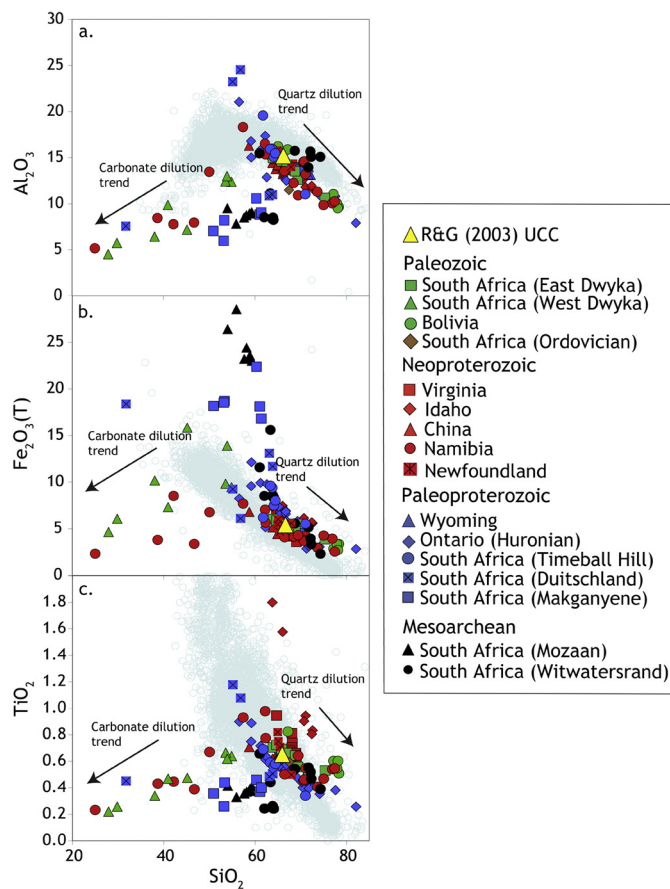


**Fig. 1.** Harker variation diagrams for glacial diamictites, showing major compositional variations. Andean volcanic arc rocks from GEOROC ([georoc.mpch-mainz.gwdg.de](http://georoc.mpch-mainz.gwdg.de); see Appendix A for full dataset and references) are shown in order to compare expected igneous differentiation trends to trends shown by the diamictites. The main trends in (a) and (b) reflect a combination of quartz dilution and differences in provenance while the trend directed towards low SiO<sub>2</sub> values is due to carbonate dilution. (c) High TiO<sub>2</sub> in some diamictites is likely a reflection of significant contributions from A-type granites. UCC model composition of Rudnick and Gao (2003) is also shown for comparison.

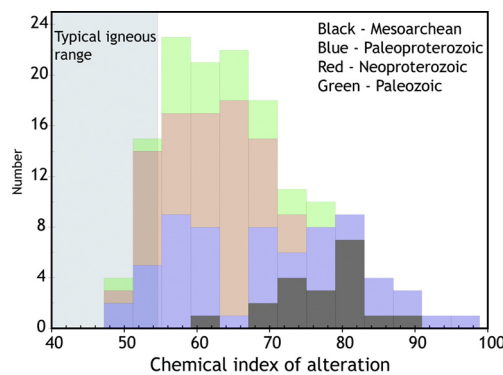


**Fig. 2.** Histogram of CIA values for the glacial diamictites. CIA – Chemical index of alteration = molar Al<sub>2</sub>O<sub>3</sub>/(Al<sub>2</sub>O<sub>3</sub> + K<sub>2</sub>O + Na<sub>2</sub>O + CaO\*) (Young and Nesbitt, 1982), where CaO\* is corrected to remove the contribution of carbonate and apatite (see text for details). (Bars are stacked in order of decreasing age from bottom to top. See web version of article for color).

Mesoarchean localities mainly showing enriched levels of these transition metals. In addition to the overall relative abundance differences in transition metals, fractionations appear between Cr and V and their neighboring transition metals, and the sign of these fractionations also largely depends on age: diamictites from most Neoproterozoic and younger localities show relative depletions of Cr and V, while those from the older localities show rel-

ative enrichments. The degree of enrichment or depletion can be quantified by calculating the differences between Cr, V, and Mo, and their elemental neighbors in Figs. 3 and 4 and plotting them as Cr, V, and Mo “anomalies”, with Mo/Mo\* = Mo<sub>n</sub>/(Ce<sub>n</sub>\*Pr<sub>n</sub>)<sup>0.5</sup>, V/V\* = V<sub>n</sub>/(Lu<sub>n</sub>\*Sc<sub>n</sub>)<sup>0.5</sup>, and Cr/Cr\* = Cr<sub>n</sub>/(Sc<sub>n</sub>\*Co<sub>n</sub>)<sup>0.5</sup>, as shown in Fig. 5.

## 5. Discussion

The systematic changes in the distribution of redox sensitive transition metals in the diamictites during and after the Paleo-proterozoic likely reflect the growing geochemical signature of oxidative weathering that has been imparted on the UCC. However, before considering this in detail, we must first establish the general nature and origin of the weathering signature borne by the diamictites and consider whether other secular geochemical changes may have generated the observed variations.

### 5.1. Pervasive weathering signature in the UCC

One of the rationales for exploring the use of glacial diamictite geochemistry to trace the composition of the UCC is that, unlike shales, chemical weathering is not an intrinsic process associated with diamictite genesis (Bahlburg and Dobrzinski, 2011; Dobrzinski et al., 2004; Nesbitt and Young, 1996; Young and Nesbitt, 1999). Thus, glacial diamictites may provide insights into the average concentrations of more soluble elements in the UCC. However, most of the diamictites examined here have CIA values above those of igneous rocks (Figs. 2 and 6; see also Fig. A2). Furthermore, nearly all of the diamictites (save those containing significant detrital carbonate components) are strongly depleted in Sr (Figs. 3 and 6; see also Fig. A3), a highly soluble element and one of the first to be removed from silicate rocks during chemical weathering due to its presence in disseminated hydrothermal or metamorphic carbonate veins (Jacobson and Blum, 2000; White et al., 1999). Although intracrustal magmatic differentiation may also lead to Sr depletion in the UCC due to its partitioning into cumulate or residual feldspar, such differentiation should also lower Eu/Eu\*. Because we do not see a strong correlation between Eu/Eu\* and Sr/Sr\* (Fig. A4), we conclude that chemical weathering is likely the main cause of the prevalent Sr depletions seen in the diamictites and we can use Sr/Sr\* (defined as Sr<sub>n</sub>/(Ce<sub>n</sub>\*Nd<sub>n</sub>)<sup>0.5</sup>) as an indicator of incipient weathering, along with the CIA (Fig. 6).

The chemical weathering signature that is so pervasive in the diamictites is unlikely to be produced by post-depositional processes insofar as the diamictites were deposited rapidly in marginal marine settings and subsequently buried by conformable sedimentary rocks prior to uplift (Table 1). Furthermore, we observed no evidence of paleosols in any of the sampled deposits, and sampling from the top to the interior of selected deposits (e.g., Nantuo, Duitschland) reveal no systematic changes in soluble element concentrations (Fig. A5) typical of weathering horizons (e.g., Liu et al., 2013). Moreover, chemical weathering during glacial transport is expected to be minimal, given that weathering reactions are exponentially correlated with temperature (Walker et al., 1981), and temperatures during glacial erosion and transport were undoubtedly low. Thus, we conclude that the weathering signature recorded in the diamictites is inherited from the UCC over which the glaciers traversed.

### 5.2. Diamictites and the temporal evolution UCC composition

In order to use the composition of the fine-grained matrix of glacial diamictites to track the compositional evolution of the upper crust through time, it is important to establish that these samples provide a robust average of large tracts of UCC for the

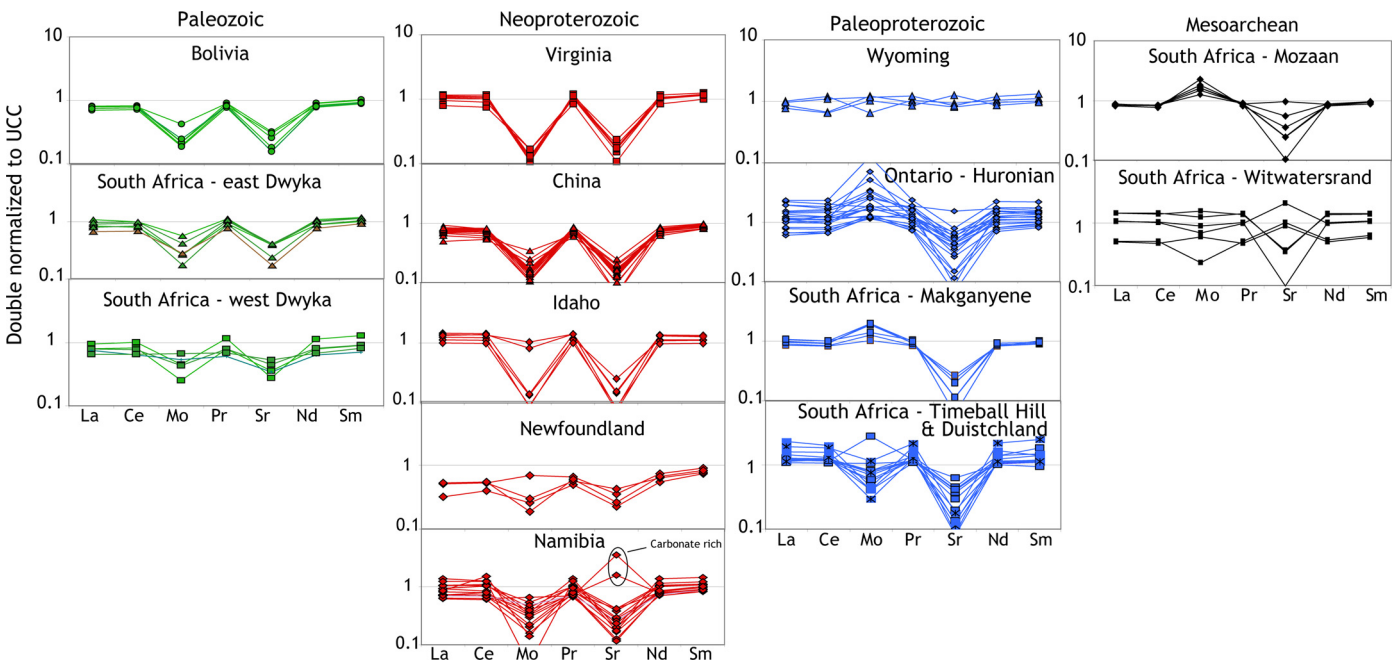


**Fig. 3.** Normalized abundance diagrams showing the light rare earth elements (LREEs), Sr and Mo in individual glacial diamictite samples from different localities, sorted by increasing depositional age, from left to right. Elemental abundances are multiplied by the ratio of the measured sample Y content to the average Y abundance of the upper continental crust (UCC) to reduce the effects of quartz and carbonate dilution, and then these abundances are normalized to the average UCC (Rudnick and Gao, 2003). Mo is expected to have a similar partition coefficient as Pr during extraction of melts from the mantle (Newsom and Palme, 1984), whereas Sr has a similar partition coefficient to Nd (McDonough and Sun, 1995). Paleoproterozoic and Mesoarchean samples show either similar behavior between LREEs and Mo, or Mo enrichment, whereas Mo is depleted in younger samples. Nearly all samples show depletion of Sr, which is lost to solution during the incipient stages of weathering (see text). Two carbonate-rich samples from Namibia are enriched in Sr. The brown trace in the Paleozoic east Dwyka plot is the sole Ordovician sample analyzed. Duitschland samples are distinguished from Timeball Hill by the presence of asterisks in the boxes of the former. (See web version of article for color figure.)

elements of interest. There is significant inter-formation geochemical variability and a lesser amount of intra-formation variability within our sample suite, as seen in major element compositions (Fig. 1). Much of this variability can be related to the local geology over which the glaciers flowed. For example, diamictites from the Archean Mozaan Group and Paleoproterozoic Makganyene Formation have exceptionally high  $\text{Fe}_{2}\text{O}_3(\text{T})$  contents and relatively low  $\text{SiO}_2$  and  $\text{Al}_2\text{O}_3$  contents (Fig. 1b), likely reflecting the influence of iron formation in their provenance. In contrast, diamictite samples from the Archean Witwatersrand Supergroup have some of the highest MgO contents (without corresponding high LOI that would indicate Mg-carbonate), accompanied by low  $\text{Al}_2\text{O}_3$  and high Mg#, reflecting a komatiite-dominated provenance. The diamictites from the Neoproterozoic Ghuab Formation (Namibia) have very high CaO and loss on ignition (LOI), reflecting a large carbonate component in their provenance. Finally, high  $\text{TiO}_2$ ,  $\text{P}_2\text{O}_5$  and Y contents in the diamictites in the Neoproterozoic Pocatello (Idaho) and Konnarock (Virginia) formations reflect a significant proportion of A-type granites in the source region (Fig. 1c). From these observations it is clear that local provenance can exert a control on the major element composition of the samples.

Despite these regional variations, systematic changes in relative trace element abundances correlate with the age of deposit. For example, Mesoarchean and early Paleoproterozoic diamictites are consistently enriched in first row transition metals relative to younger deposits (Fig. 4), especially when compared to the heavy rare earth elements, which show little variation between units. [The exception to this trend is the western Dwyka Group, which closely mirrors the Archean samples and contains a detrital zircon population consisting only of early Paleoproterozoic and Archean zircons (Gaschnig et al., unpublished data).] This observation reflects a greater proportion of mafic to ultramafic lithologies in the Archean upper crust, as has been previously deduced from shale

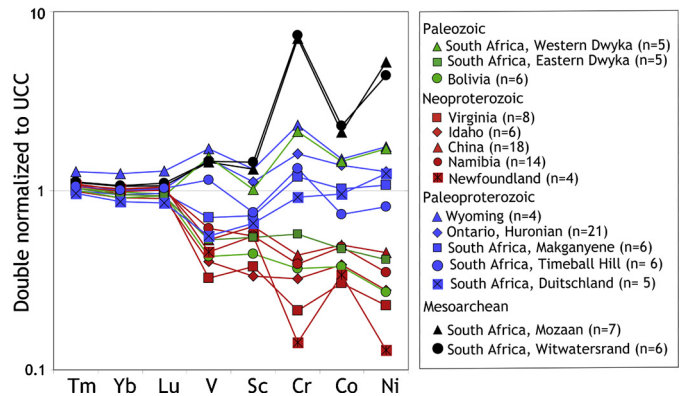


**Fig. 4.** Abundance normalized diagrams of the HREEs and transition metals. Each pattern represents the log-normal average for the locality. Normalization scheme as in Fig. 3. The overall depletion in transition metals seen in the Neoproterozoic and younger samples reflects the secular evolution of the average composition of the UCC (Condie, 1993; Taylor and McLennan, 1985). Note that Cr and V are slightly enriched relative to their neighbors for Paleoproterozoic and Mesoarchean samples, whereas they show complementary depletions in the younger samples. The similarity of the western Dwyka samples to the Paleoproterozoic and Archean samples is a reflection of purely >2.0 Ga provenance (Gaschnig, unpublished data). (See web version of article for color figure.)

(Taylor and McLennan, 1985; Condie, 1993) and outcrop-based studies of the average composition of the UCC (Eade and Fahrig, 1971, 1973; Condie, 1993). In addition to the overall changes in abundances, Ni/Co ratios decrease systematically from the Archean to the Neoproterozoic (Fig. 4), as has been observed in shales (Condie, 1993). The similarity in the secular evolution of shales and glacial diamictites suggest that the latter can be faithful recorders of the changing composition of the UCC, despite the fact that they can be influenced by regional geology.

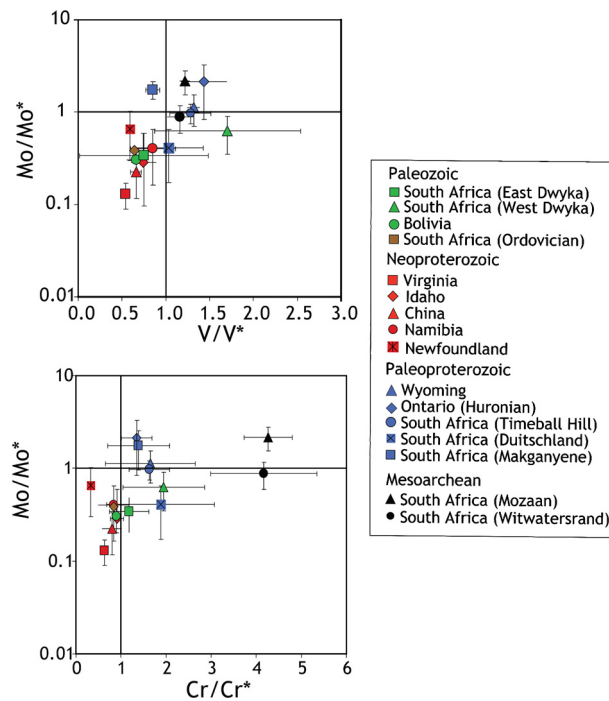


**Fig. 5.** Enrichment and depletion trends for redox sensitive transition metals in average diamictites from a given geographic region. Error bars are 1 sigma standard deviation. Ratios reflect enrichment or depletion of Mo, V, and Cr relative to elements with similar compatibility when normalized to UCC, where  $Mo^* = (Ce_n * Pr_n)^{0.5}$ ,  $V^* = (Lu_n * Sc_n)^{0.5}$ , and  $Cr^* = (Sc_l * Co_n)^{0.5}$ . Samples are colored coded by age (green = Paleozoic; red = Neoproterozoic; blue = Paleoproterozoic; Mesoarchean = black). Mesoarchean and Paleoproterozoic diamictites are generally enriched in these redox-sensitive transition metals, whereas younger diamictites are depleted. The unusually large enrichment in Cr seen in the Mesoarchean samples may reflect the prevalence of komatiites in the Archean UCC (Condé, 1993; Taylor and McLennan, 1985) in addition to its low solubility under anoxic weathering conditions. (See web version of article for color figure.)

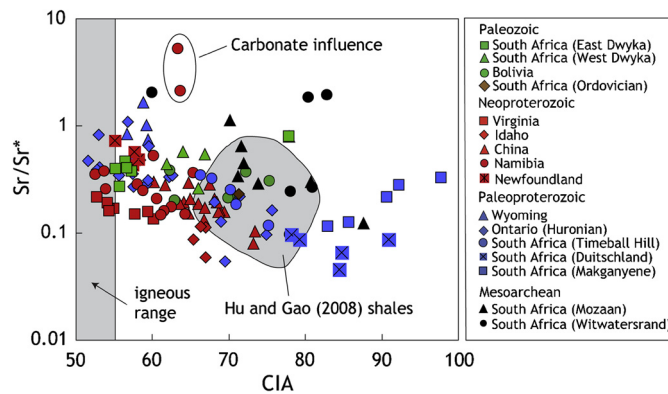


**Fig. 6.** Chemical index of alteration (CIA) vs. Sr depletion factor ( $Sr/Sr^* = (Ce_n * Nd_n)^{0.5}$ ) for the diamictites. CIA values between 40 and 55 are typical of fresh igneous rocks. The CIA is less than 70 for the majority of samples, but nearly all show depletion in Sr, suggesting that all samples have been influenced by chemical weathering. Sr enrichment seen in some of the Neoproterozoic Namibian samples is linked to significant carbonate content. The gray field represents post-Archean shales studied by Hu and Gao (2008), and includes some post-Archean Australian shale (PAAS, Nance and Taylor, 1976) samples, as well as samples from eastern China. (See web version of article for color figure.)

### 5.2.1. Transition metals systematics: UCC differentiation vs surface redox effects

The redox sensitive transition metals V, Cr, and Mo can provide important information about the availability of oxygen in ancient sedimentary environments, and in the diamictites, these elements tend to decrease systematically in relative and absolute abundance

with time (Figs. 3, 4, and 5). However, these elements are also affected by igneous differentiation, so it is important to establish expected igneous differentiation trends in order to separate the effects of the general shift in the UCC towards more felsic compositions with time from changes related to redox effects. To do this, we consider the ratios of interest in igneous rocks to see if there are systematic changes in genetically-related igneous suites that would imply different bulk partition coefficients during differentiation.

We start with the simplest case of Ni/Co, since both elements are isovalent (2+) and therefore should not be influenced by oxidative weathering. As noted above, Ni/Co decreases with time in both shales and glacial diamictites, and, by inference, the average UCC. We see that Ni/Co also decreases systematically in igneous calc-alkaline suites as  $SiO_2$  increases (Fig. 7a). Given that Ni shows the largest dispersion of normalized concentrations within the diamictites (Fig. 4), we can use normalized Ni values ( $Ni_{norm}$ ) as a sensitive indicator of the degree of differentiation of the UCC, as recorded by the diamictites. The Ni/Co ratio of the diamictites shows a good correlation with  $Ni_{norm}$  (Fig. 8a), consistent with the hypothesis that intracrustal differentiation is responsible for the temporal change in Ni/Co.

Like Ni/Co, Cr/Sc decreases systematically with  $SiO_2$  in igneous suites (Fig. 7b), and also shows a good correlation with  $Ni_{norm}$  (Fig. 8b) suggesting that intracrustal differentiation can explain the lower Cr/Cr\* in Neoproterozoic and younger glacial diamictites. However, given the high solubility of  $Cr^{6+}$ , it is also possible that oxidative weathering contributed to the Cr depletion seen in the UCC over time. Because both processes act to lower Cr/Cr\*, we cannot differentiate between them, and both may have played a role in the temporal evolution of Cr concentration in the UCC. Indeed, the increase in Cr seen in black shales through time mimics the increase in Mo, suggesting that Cr was also lost from the continents after the rise of oxygen (Reinhard et al., 2013).

In contrast to Ni/Co and Cr/Sc, V/Sc does not change systematically in igneous suites (Fig. 7c, Li and Lee, 2004), suggesting that these two elements share similar bulk partition coefficients during intracrustal differentiation. Moreover, a very poor correlation exists between V/Sc and  $Ni_{norm}$  (Fig. 8c). These observations suggest that the depletion of V in glacial diamictites from the Neoproterozoic onward reflects the influence of oxidative weathering on the UCC. Similarly, although relatively few Mo analyses exist for igneous rocks world-wide, these data suggest either no change or a slight increase in Mo/Ce with differentiation, which is the opposite of the trend that we observe in the diamictites (Fig. 7d).

In summary, the transition metal abundances document systematic changes in the average composition of the UCC. Higher Ni/Co, Cr/Cr\* and overall transition metal concentrations in Archean and Paleoproterozoic diamictites relative to Neoproterozoic and younger diamictites document a change from upper crust dominated by basalt and komatiite, to one dominated by granitic rocks. In contrast, the behavior of vanadium can be confidently linked to oxidative weathering. Based on V/V\*, Archean diamictites and all but the South African Paleoproterozoic diamictites carry a weathering signature that developed in the absence of oxygen (i.e.,  $V/V^* \geq 1$ ), whereas all Neoproterozoic and Paleozoic diamictites (with the exception of the western Dwyka, and the carbonate-rich Ghaub samples) carry a weathering signature that developed in the presence of oxygen ( $V/V^* < 1$ ). The South African Paleoproterozoic diamictites show variable behavior: Timeball Hill deposits have  $V/V^* > 1$ , whereas the Duitschland and Makganyene diamictites have  $V/V^* < 1$ . Curiously, the Timeball Hill formed post-GOE, whereas Duitschland formed pre-GOE (Bekker et al., 2001, 2004; Guo et al., 2009); the depositional age of the Makganyene diamictites is controversial

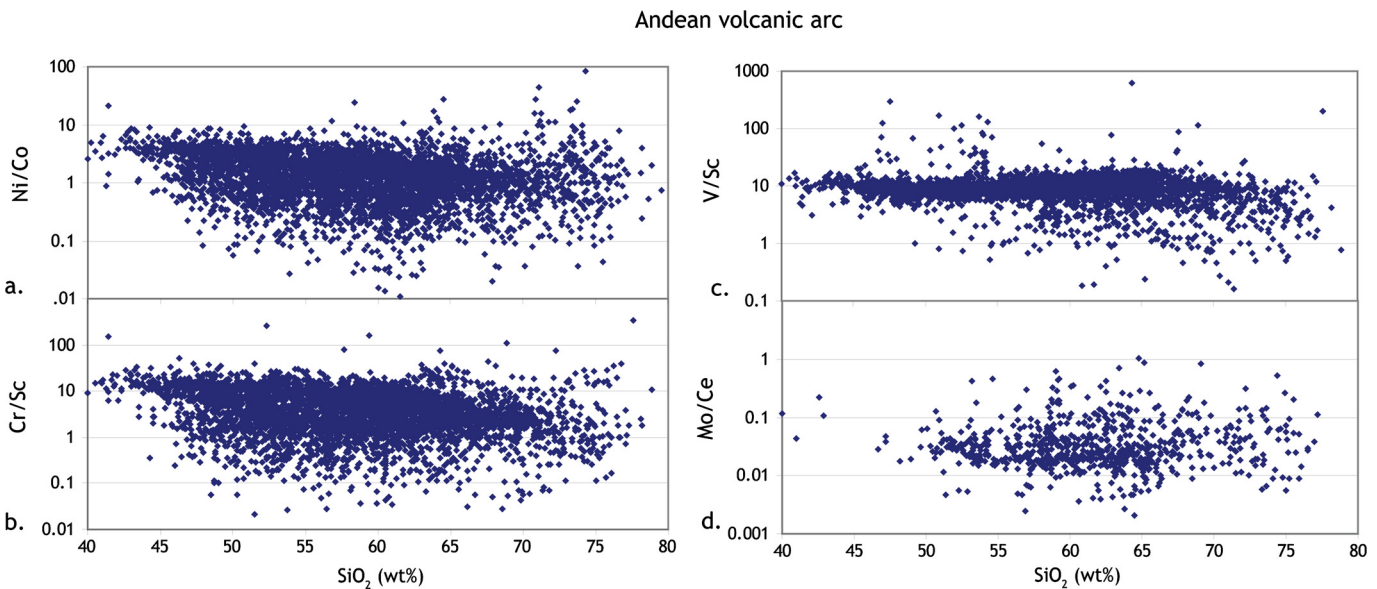


**Fig. 7.** Examples of igneous differentiation trends for transition metals in the Andean volcanic arc. Data from GEOROC. (a) Ni/Co and (b) Cr/Sc both decrease with increasing differentiation whereas V/Sc and Mo/Ce lack systematic trends. This indicates that the secular shift in V and Mo seen in the diamictites is unlikely to be due to primary igneous processes but instead due to the increasing importance of oxidative weathering.

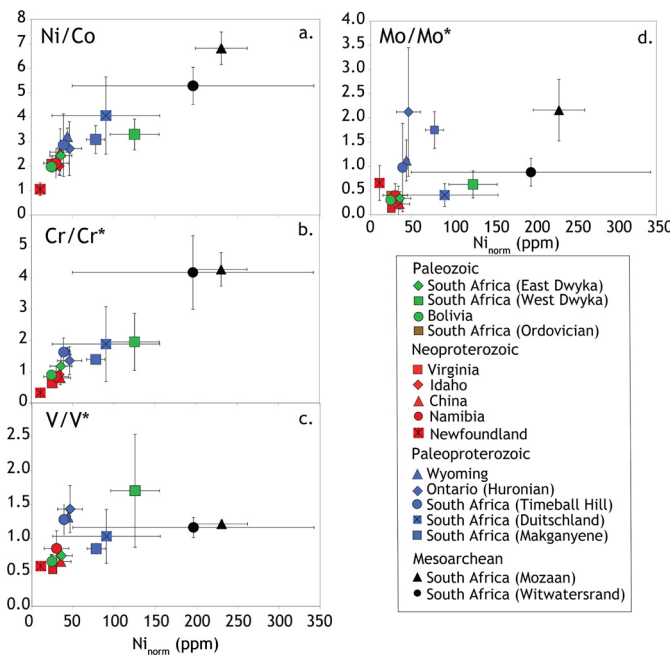


**Fig. 8.**  $\text{Ni}_{\text{norm}}$  vs. Ni/Co, Cr/Cr\*, V/V\* and Mo/Mo\*.  $\text{Ni}_{\text{norm}}$  is Ni concentration normalized to Rudnick and Gao (2003) average UCC  $\text{Al}_2\text{O}_3$  of 15.26% ( $\text{Ni}_{\text{norm}} = 15.26/\text{Al}_2\text{O}_3\text{measured} * \text{Ni}_{\text{measured}}$ ). Good correlation between  $\text{Ni}_{\text{norm}}$  and Ni/Co and Cr/Cr\* is interpreted as an intracrustal differentiation trend due to the similar igneous partition coefficients between Ni and Cr. However,  $\text{Ni}_{\text{norm}}$  is decoupled from V/V\* and Mo/Mo\* due to the influence of oxidative weathering on V and Mo behavior. (See web version of article for color figure.)

(Moore et al., 2001; Coetze et al., 2006; Hoffman, 2013) (Table 1). This unexpected pre-GOE oxidative weathering signature is explored further in the next section.

### 5.2.2. Mo and the rise of oxygen

Mo/Mo\* shows an even more dramatic secular shift in the diamictites than V/V\*. Moreover, a lack of correlation between Mo/Mo\* and  $\text{Ni}_{\text{norm}}$  within the diamictites (Fig. 8d) suggests that the main cause of the Mo depletion in the UCC is the onset of oxidative weathering. All Neoproterozoic and younger glacial diamic-

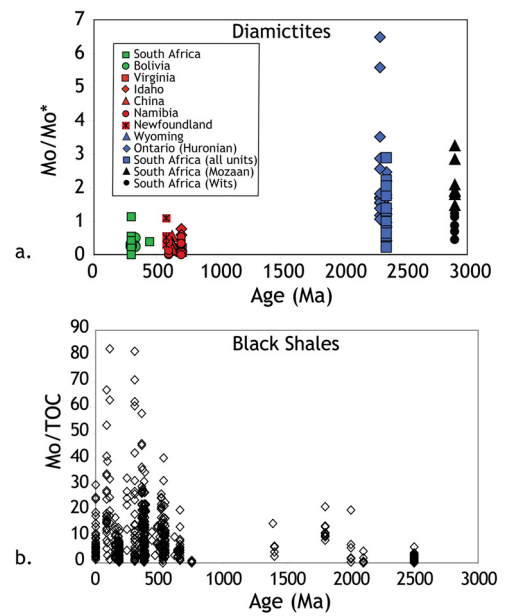


**Fig. 9.** Mo in (a) diamictites and (b) black shales vs age. Black shale data from Scott et al. (2008) and Sahoo et al. (2012). There is a strong inverse relationship between the diamictites and shales, indicating the progressive loss of Mo from the continents and accumulation in the ocean basins as oxygen levels rose.

tites show Mo depletion (Fig. 9) and the opposite trend is seen in black shales (Sahoo et al., 2012; Scott et al., 2008). These complementary trends indicate the progressive loss of Mo from the continents and its deposition in the ocean basins as atmospheric oxygen rose. In contrast, all Archean and many Paleoproterozoic diamictites are not depleted in Mo and some even show Mo enrichments (Fig. 3). Mo enrichment may reflect the complementarity between the older and younger UCC compositions, but, in the strongly enriched Huronian samples may also reflect diagenetic enrichment of Mo (though none of the samples have significant organic carbon concentrations, which is generally linked to authigenic uptake of Mo, and there is no correlation between Mo/Mo\* and total organic carbon, Fig. A6).

The Paleoproterozoic glacial deposits warrant particular scrutiny, as the depositional ages for these units span the GOE, as marked by the disappearance of MIF in sulfur isotopes. None of the samples from the Huronian Supergroup, Ontario (Ramsey Lake, Bruce or Gowganda diamictites and Pecors dropstone argillites) are depleted in Mo, yet the Gowganda diamictite is interpreted as having been deposited following the GOE (Papineau et al., 2007). These deposits sample predominantly Neoarchean crust, based on their detrital zircon populations (Gaschnig et al., unpublished data), and have some of the lowest CIA values within the entire sample set (Table 2, Fig. 2), although Sr depletions and CIA values above 55, in some samples, suggests that the source terrain was slightly weathered. It is possible that the lack of oxidative weathering signature simply reflects their provenance (Archean crust moderately weathered under an anoxic atmosphere) and does not record atmospheric oxygen levels at the time of their deposition.

In contrast to the Huronian diamictites, which have  $\text{Mo/Mo}^* \geq 1$ , Paleoproterozoic diamictites from South Africa show quite variable behavior with respect to Mo. All samples are derived from a heavily weathered provenance, based on their high CIA (mean = 79) and low  $\text{Sr/Sr}^*$  (mean = 0.2). The Timeball Hill diamictites, deposited post-GOE (Bekker et al., 2004) have low  $\text{Mo/Mo}^*$  (mean = 0.6), consistent with an oxidative weathering imprint on their provenance. The Makganyene diamictites, of uncertain depositional age with respect to the GOE, have  $\text{Mo/Mo}^*$  above 1. This could reflect their deposition before the GOE, or, like the Gowganda diamictites of Ontario, may simply reflect a provenance of Archean crust that was weathered in the absence of  $\text{O}_2$ . Finally, and most intriguingly, the Duitschland diamictite, deposited pre-GOE (Bekker et al., 2004) have very low  $\text{Mo/Mo}^*$  (mean = 0.4) and some of the lowest  $\text{Sr/Sr}^*$  (mean = 0.08). Given the absence of any evidence of post-depositional weathering in the drill core samples (see Fig. A5 and discussion in Section 5.1), these observations record significant pre-GOE oxidative weathering of the protolith. Several recent studies also document a “whiff” of oxygen at least 150 Ma before the GOE (Anbar et al., 2007; Kaufman et al., 2007; Lyons et al., 2014, and references therein), and possibly even earlier (Crowe et al., 2013; Mukhopadhyay et al., 2014). The Duitschland diamictite provides strong evidence for intense weathering ( $\text{CIA} = 78$  to 91,  $\text{Sr/Sr}^* = 0.05$  to 0.1) in the presence of atmospheric  $\text{O}_2$  ( $\text{Mo/Mo}^* = 0.2$  to 0.6,  $\text{V/V}^* = 0.5$  to 1.5) prior to its deposition (constrained to be between 2.31 and 2.48 Ga; Rasmussen et al., 2013). Given the strongly attenuated MIF signal after 2.5 Ga (Fig. 2 of Lyons et al., 2014), it may be that the GOE cannot be uniquely traced by MIF, as sediment cannibalization leads to “leaking” of the MIF signal to younger rocks (Reinhard et al., 2013; Lyons et al., 2014). Finally, the strong signal of oxidative weathering in the Duitschland diamictite and the lack of such a signature in the Huronian diamictites, including the possibly correlative Ramsay Lake Formation (Rasmussen et al., 2013), suggests either that the Duitschland is younger than the Ramsay Lake, or, perhaps more likely, that the Ramsay Lake reflects a provenance weathered in the Archean, with little input of oxidatively weathered UCC.

## 6. Conclusions

The geochemistry of glacial diamictites from the four recognized pre-Cenozoic glacial intervals provide insight into the average composition of the Earth's upper continental crust and closely parallel the temporal trends seen in other UCC proxies, such as enrichment of first row transition metals in Paleoproterozoic and Archean samples, indicating that the UCC was more mafic in the Archean. All diamictites bear a chemical weathering signature, but the nature of this signature differs in a systematic and secular fashion. The redox sensitive elements Mo, V, and Cr show normal to enriched levels in all of the Archean and most of the Paleoprotero-

zoic diamictites but are strongly depleted in Neoproterozoic and Paleozoic diamictites. While some of the change in Cr behavior may be due to changes in the primary composition of the UCC, the progressive depletion in V and Mo reflect the rise of oxidative weathering of the continents, leading to the transfer of these elements from the continents to the ocean basins. Although oxidative weathering was clearly pervasive after the Paleoproterozoic, the differences in redox sensitive metals between different Paleoproterozoic formations suggest that oxygen levels may have risen substantially prior to the GOE.

## Acknowledgements

This research was supported by NSF EAR-1321954, NSF FESD EAR-1338810, and a grant from the State Key Laboratory of Geological Processes and Mineral Resources at China University of Geosciences in Wuhan. We thank Nic Beukes, Paul Link, Lian Zhou, Charlie Hoffmann, and Guy Narbonne for help with sampling and geologic interpretation; Andrey Bekker and Linda Kah for feedback on the data; Heidi Anderson for providing the Bolivian samples; Richard Ash, Igor Puchtel, Zhang Wen, and Lin Lin for help with analytical work; Mike Ream, Will Junkin, and Kalle Hantsoo for help with sample processing; and Lew Ashwal and Sue Webb for providing accommodations in Johannesburg during our South African field work. This manuscript was significantly improved by reviews from Scott McLennan, Catherine Chauvel, and Francis Jenner.

## Appendix A. Supplementary material

Supplementary material related to this article can be found online at <http://dx.doi.org/10.1016/j.epsl.2014.10.002>.

## References

- Anbar, A.D., Duan, Y., Lyons, T.W., Arnold, G.L., Kendall, B., Creaser, R.A., Kaufman, A.J., Gordon, G.W., Scott, C., Garvin, J., Buick, R., 2007. A whiff of oxygen before the Great Oxidation Event? *Science* 317 (5846), 1903–1906.
- Armstrong, R.A., Compston, W., Retief, E.A., Williams, I.S., Welke, H.J., 1991. Zircon ion microprobe studies bearing on the age and evolution of the Witwatersrand triad. *Precambrian Res.* 53, 243–266.
- Asael, D., Tissot, F., Reinhard, C.T., Rouxel, O., Dauphas, N., Lyons, T.W., Ponzevere, E., Liorzou, C., Cheron, S., 2013. Coupled molybdenum, iron and uranium stable isotopes as oceanic paleoredox proxies during the Paleoproterozoic Shunga Event. *Chem. Geol.* 362, 193–210.
- Bahubalgi, H., Dobrzynski, N., 2011. A review of the chemical index of alteration (CIA) and its application to the study of Neoproterozoic glacial deposits and climate transitions. In: Arnaud, E., Halverson, G.P., Shields-Zhou, G. (Eds.), *The Geological Record of Neoproterozoic Glaciations. Memoir*. Geological Society of London, London, pp. 81–92.
- Bekker, A., Kaufman, A.J., 2007. Oxidative forcing of global climate change: a biogeochemical record across the oldest Paleoproterozoic ice age in North America. *Earth Planet. Sci. Lett.* 258, 486–499.
- Bekker, A., Kaufman, A.J., Karhu, J.A., Beukes, N.J., Swart, Q.D., Coetzee, L.L., Eriksson, K.A., 2001. Chemostratigraphy of the Paleoproterozoic Duitschland Formation, South Africa: implications for coupled climate change and carbon cycling. *Am. J. Sci.* 301, 261–285.
- Bekker, A., Karhu, J.A., Eriksson, K.A., Kaufman, A.J., 2003. Chemostratigraphy of Paleoproterozoic carbonate successions of the Wyoming Craton: tectonic forcing of biogeochemical change? *Precambrian Res.* 120 (3–4), 279–325.
- Bekker, A., Holland, H.D., Wang, P.L., Rumble, D., Stein, H.J., Hannah, J.L., Coetzee, L.L., Beukes, N.J., 2004. Dating the rise of atmospheric oxygen. *Nature* 427 (6970), 117–120.
- Beukes, N.J., Dorland, H., Gutzmer, J., Nedachi, M., Ohmoto, H., 2002. Tropical laterites, life on land, and the history of atmospheric oxygen in the Paleoproterozoic. *Geology* 30 (6), 491–494.
- Bowring, S.A., Myrow, P.M., Landing, E., Ramezani, J., 2003. Geochronological constraints on terminal Neoproterozoic events and the rise of metazoans. In: *NASA Astrobiology Institute General Meeting Abstracts*, pp. 113–114.
- Calvert, S.E., Pedersen, T.F., 1993. Geochemistry of recent oxic and anoxic marine sediments: implications for the geological record. *Mar. Geol.* 113 (1–2), 67–88.
- Canil, D., Lacourse, T., 2011. An estimate for the bulk composition of juvenile upper continental crust derived from glacial till in the North American Cordillera. *Chem. Geol.* 284 (3–4), 229–239.

- Carte, S.L., Eyles, N., 2011. The deep-marine glaciogenic Gaskiers Formation, Newfoundland, Canada. In: Arnaud, E., Halverson, G.P., Shields-Zhou, G. (Eds.), The Geological Record of Neoproterozoic Glaciations, Memoirs, vol. 36. Geological Society, London, pp. 467–473.
- Coetze, L.L., Beukes, N.J., Gutzmer, J., Kakegawa, T., 2006. Links of organic carbon cycling and burial to depositional depth gradients and establishment of a snowball Earth at 2.3 Ga. Evidence from the Timeball Hill Formation, Transvaal Supergroup, South Africa. *South African Journal of Geology* 109, 109–122.
- Condie, K.C., 1993. Chemical composition and evolution of the upper continental crust: contrasting results from surface samples and shales. *Chem. Geol.* 104 (1–4), 1–37.
- Crowe, S.A., Dossing, L.N., Beukes, N.J., Bau, M., Kruger, S.J., Frei, R., Canfield, D.E., 2013. Atmospheric oxygenation three billion years ago. *Nature* 501 (7468), 535–538.
- Crowell, J.C., 1999. Pre-Mesozoic Ice Ages: their bearing on understanding the climate system. *Mem. Geol. Soc. Amer.* 192, 1–112.
- Dobrzinski, N., Bahlburg, H., Strauss, H., Zhang, Q., 2004. Geochemical proxies applied to the Neoproterozoic glacial succession on the Yangtze Platform, South China. In: Jenkins, G.S., McMenamin, M.A.S., McKay, C.P., Sohl, L. (Eds.), The Extreme Proterozoic: Geology, Geochemistry, and Climate. Monograph. AGU, pp. 13–32.
- Eade, K.E., Fahrig, W.F., 1971. Chemical evolutionary trends of continental plates – preliminary study of the Canadian Shield. *Geol. Surv. Can. Bull.* 179, 1–51.
- Eade, K.E., Fahrig, W.F., 1973. Regional, lithological, and temporal variation in the abundances of some trace elements in the Canadian Shield. *Geol. Surv. Can. Paper* 72, 1–46.
- Farquhar, J., Bao, H., Thiemens, M., 2000. Atmospheric influence of Earth's earliest sulfur cycle. *Science* 289 (5480), 756–758.
- Frimmel, H.E., 2011. The Kaigas and Numees formations, Port Nolloth Group, in South Africa and Namibia. In: Arnaud, E., Halverson, G.P., Shields-Zhou, G. (Eds.), The Geological Record of Neoproterozoic Glaciations, Memoirs, vol. 36. Geological Society, London, pp. 223–231.
- Gaschnig, R.M., Rudnick, R.L., McDonough, W.F., 2014. Standard addition ICP-MS characterization of selected chalcophile and siderophile elements (Ga, Ge, Mo, Ag, Cd, In, Sn, Sb, W, Ti, and Bi) in USGS whole-rock reference materials. *Geostand. Geoanal. Res.* (submitted for publication).
- Gay, A.L., Grandstaff, D.E., 1980. Chemistry and mineralogy of Precambrian paleosols at Elliot Lake, Ontario, Canada. *Precambrian Res.* 12 (1–4), 349–373.
- Gilleaudeau, G.J., Kah, L.C., 2013. Oceanic molybdenum drawdown by Epeiric sea expansion in the Mesoproterozoic. *Chem. Geol.* 356, 21–37.
- Goldschmidt, V.M., 1933. Grundlagen der quantitativen geochemie. *Fortschr. Mineral. Krystallogr. Petrograph.* 17, 112–156.
- Grandstaff, D.E., 1980. Origin of uraniferous conglomerates at Elliot Lake, Canada and Witwatersrand, South Africa: implications for oxygen in the Precambrian atmosphere. *Precambrian Res.* 13, 1–26.
- Grandstaff, D.E., Edelman, M.J., Foster, R.W., Zbinden, E., Kimberley, M.M., 1986. Chemistry and mineralogy of Precambrian paleosols at the base of the Dominion and Pongola Groups (Transvaal, South Africa). *Precambrian Res.* 32 (2–3), 97–131.
- Guo, Q., Strauss, H., Kaufman, A.J., Schroder, S., Gutzmer, J., Wing, B., Baker, M.A., Bekker, A., Jin, Q., Kim, S., Farquhar, J., 2009. Reconstructing Earth's surface oxidation across the Archean-Proterozoic transition. *Geology* 37 (5), 399–402.
- Guy, B.M., Beukes, G.J., Gutzmer, J., 2010. Paleoenvironmental controls on the texture and chemical composition of pyrite from non-conglomeratic sedimentary rocks of the Mesoarchean Witwatersrand Supergroup, South Africa. *South African Journal of Geology* 113, 195–228.
- Hambrey, M.J., 1985. The Late Ordovician-Early Silurian glacial period. *Palaeogeogr. Palaeoclimatol. Palaeoecol.* 51 (1–4), 273–289.
- Hoffman, P.F., 2011. Strange bedfellows; glacial diamictite and cap carbonate from the Marinoan (635 Ma) glaciation in Namibia. *Sedimentology* 58, 57–119.
- Hoffman, P.F., 2013. The Great Oxidation and a Siderian snowball Earth: MIF-S based correlation of Paleoproterozoic glacial epochs. *Chem. Geol.* 362, 143–156.
- Hoffman, P.F., Li, Z.-X., 2009. A Palaeogeographic context for Neoproterozoic glaciation. *Palaeogeogr. Palaeoclimatol. Palaeoecol.* 277, 158–172.
- Hoffmann, K.H., Condon, D.J., Bowring, S.A., Crowley, J.L., 2004. U-Pb zircon date from the Neoproterozoic Ghaub Formation, Namibia: constraints on Marinoan glaciation. *Geology* 32, 817–820.
- Holland, H.D., 2006. The oxygenation of the atmosphere and oceans. *Philos. Trans. R. Soc. Lond. B, Biol. Sci.* 361 (1470), 903–915.
- Houston, R.S., Karlstrom, K.E., Graff, P.J., Flurkey, A.J., 1992. New stratigraphic subdivisions and redefinition of subdivisions of Late Archean and Early Proterozoic metasedimentary and metavolcanic rocks of the Sierra Madre and Medicine Bow Mountains, southern Wyoming. In: U.S. Geological Survey Professional Paper, vol. 1520, p. 50.
- Hu, Z., Gao, S., 2008. Upper crustal abundances of trace elements: a revision and update. *Chem. Geol.* 253, 205–221.
- Isbell, J.L., Cole, D.I., Catuneanu, O., 2008. Carboniferous-Permian glaciation in the main Karoo Basin, South Africa: stratigraphy, depositional controls, and glacial dynamics. In: Fielding, C.R., Frank, T.D., Isbell, J.L. (Eds.), Resolving the Late Paleozoic Ice Age in Time and Space. In: Geological Society of America Special Paper, vol. 441, pp. 71–82.
- Jacobson, A.D., Blum, J.D., 2000. Ca/Sr and  $^{87}\text{Sr}/^{86}\text{Sr}$  geochemistry of disseminated calcite in Himalayan silicate rocks from Nanga Parbat: influence on river-water chemistry. *Geology* 28 (5), 463–466.
- Kaufman, A.J., Johnston, D.T., Farquhar, J., Masterson, A., Lyons, T.W., Bates, S., Anbar, A.D., Arnold, G.L., Garvin, J., Buick, R., 2007. Late Archean biosphere oxygenation and atmospheric evolution. *Science* 317, 1900–1903.
- Kaufman, A.J., Sial, A.N., Frimmel, H.E., Misi, A., 2009. Neoproterozoic to Cambrian Palaeoclimatic Events in Southwestern Gondwana. In: Gaucher, C., Sial, A.N., Halverson, G.P., Frimmel, H.E. (Eds.), Neoproterozoic-Cambrian Tectonics, Global Change and Evolution: A Focus on Southwestern Gondwana. In: Developments in Precambrian Geology, vol. 16, pp. 369–388.
- Keeley, J.A., Link, P.K., Fanning, C.M., Schmitz, M.D., 2013. Pre- to synglacial rift-related Volcanism in the Neoproterozoic (Cryogenian) Pocatello Formation, SE Idaho: new SHRIMP and CA-ID-TIMS constraints. *Lithosphere* 5, 128–150.
- Kendall, B., Brennecke, G.A., Weyer, S., Anbar, A.D., 2013. Uranium isotope fractionation suggests oxidative uranium mobilization at 2.50 Ga. *Chem. Geol.* 362, 105–114.
- Kositcin, N., Krapez, B., 2004. Relationship between detrital zircon age-spectra and the tectonic evolution of the Late Archaean Witwatersrand Basin, South Africa. *Precambrian Res.* 129, 141–168.
- Le Heron, D.P., Busfield, M.E., Kamona, F., 2013. An interglacial on snowball Earth? Dynamic ice behaviour revealed in the Chuos Formation, Namibia. *Sedimentology* 60, 411–427.
- Li, Z.-X.A., Lee, C.-T.A., 2004. The constancy of upper mantle  $\text{fO}_2$  through time inferred from V/Sr ratios in basalts. *Earth Planet. Sci. Lett.* 228, 483–493.
- Liu, X., Gao, S., Diwu, C., Ling, W., 2008. Precambrian crustal growth of Yangtze Craton as revealed by detrital zircon studies. *Am. J. Sci.* 308, 421–468.
- Liu, X., Rudnick, R.L., McDonough, W.F., Cummings, M.L., 2013. Influence of chemical weathering on the composition of the continental crust: insights from Li and Nd isotopes in bauxite profiles developed on Columbia River Basalts. *Geochim. Cosmochim. Acta* 115, 73–91.
- Lyons, T.W., Reinhard, C.T., Planavsky, N.J., 2014. The rise of oxygen in Earth's early ocean and atmosphere. *Nature* 506, 307–315.
- McDonough, W.F., Sun, S.-S., 1995. Composition of the Earth. *Chem. Geol.* 120, 223–253.
- McLennan, S.M., 1993. Weathering and Global Denudation. *The Journal of Geology* 101, 295–303.
- Melezhik, V.A., Young, G.M., Eriksson, P.G., Altermann, W., Kump, L.R., Lepland, A., 2013. Huronian-age glaciation. In: Melezhik, V.A., Prave, A.R., Hanski, E.J., Fallick, A.E., Lepland, A., Kump, L.R., Strauss, H. (Eds.), Global Events and the Fennoscandian Arctic Russia – Drilling Early Earth Project. In: Reading the Archive of Earth's Oxygenation, vol. 3, pp. 1059–1109.
- Moore, J.M., Tsikos, H., Polteau, S., 2001. Deconstructing the Transvaal Supergroup, South Africa: implications for Palaeoproterozoic palaeoclimate models. *J. Afr. Earth Sci.* 33 (3–4), 437–444.
- Moore, J.M., Polteau, S., Armstrong, R.A., Corfu, F., Tsikos, H., 2012. The age and correlation of the Postmasburg Group, southern Africa: constraints from detrital zircon grains. *J. Afr. Earth Sci.* 64, 9–19.
- Mukasa, S.B., Wilson, A.H., Young, K.R., 2013. Geochronological constraints on the magmatic and tectonic development of the Pongola Supergroup (Central Region), South Africa. *Precambrian Res.* 224, 268–286.
- Mukhopadhyay, J., Crowley, Q.G., Ghosh, S., Ghosh, G., Chakrabarti, K., Misra, B., Heron, K., Bose, S., 2014. Oxygenation of the Archean atmosphere: new paleosol constraints from eastern India. *Geology* 42, 923–926.
- Nance, W.B., Taylor, S.R., 1976. Rare earth element patterns and crustal evolution. I. Australian post-Archean sedimentary rocks. *Geochim. Cosmochim. Acta* 40 (12), 1539–1551.
- Nesbitt, H.W., Young, G.M., 1996. Petrogenesis of sediments in the absence of chemical weathering: effects of abrasion and sorting on bulk composition and mineralogy. *Sedimentology* 43 (2), 341–358.
- Newsom, H.E., Palme, H., 1984. The depletion of siderophile elements in the Earth's mantle: new evidence from molybdenum and tungsten. *Earth Planet. Sci. Lett.* 69 (2), 354–364.
- Papineau, D., Mojzsis, S.J., Schmitt, A.K., 2007. Multiple sulfur isotopes from Paleoproterozoic Huronian interglacial sediments and the rise of atmospheric oxygen. *Earth Planet. Sci. Lett.* 255 (1–2), 188–212.
- Partin, C.A., Bekker, A., Planavsky, N.J., Scott, C.T., Gill, B.C., Li, C., Podkovyrov, V., Maslov, A., Konhauser, K.O., Lalonde, S.V., Love, G.D., Poulton, S.W., Lyons, T.W., 2013. Large-scale fluctuations in Precambrian atmospheric and oceanic oxygen levels from the record of U in shales. *Earth Planet. Sci. Lett.* 369–370, 284–293.
- Pavlov, A.A., Kasting, J.F., 2002. Mass-independent fractionation of sulfur isotopes in Archean sediments: strong evidence for an anoxic Archean atmosphere. *Astrobiology* 2 (1), 27–41.
- Prave, A.R., Hoffmann, K.H., Hegenberger, W., Fallick, A.E., 2011. The Witklei Group of east-central Namibia. In: Arnaud, E., Halverson, G.P., Shields-Zhou, G. (Eds.), The Geological Record of Neoproterozoic Glaciations, Memoir, vol. 36. Geological Society, London, pp. 211–216.

- Premo, W.R., Van Schmus, W.R., 1989. Zircon geochronology of Precambrian rocks in southeastern Wyoming and northern Colorado. In: Grambling, J.A., Tewksbury, B.J. (Eds.), Proterozoic Geology of the Southern Rocky Mountains. In: Geological Society of America Special Paper, vol. 235, pp. 1–12.
- Rankin, D.W., 1993. The volcanogenic Mount Rogers Formation and the overlying glaciogenic Konnarock Formation; two late Proterozoic units in southwestern Virginia. In: U.S. Geological Survey Bulletin, vol. 2029, p. 26.
- Rasmussen, B., Bekker, A., Fletcher, I.R., 2013. Correlation of Paleoproterozoic glaciations based on U-Pb zircon ages for tuff beds in the Transvaal and Huronian Supergroups. *Earth Planet. Sci. Lett.* 382, 173–180.
- Reinhard, C.T., Raiswell, R., Scott, C., Anbar, A.D., Lyons, T.W., 2009. A Late Archean sulfidic sea stimulated by early oxidative weathering of the continents. *Science* 326 (5953), 713–716.
- Reinhard, C.T., Planavsky, N.J., Lyons, T.W., 2013. Long-term sedimentary recycling of rare sulphur isotope anomalies. *Nature* 497 (7447), 100–103.
- Roscoe, S.M., 1973. The Huronian Supergroup, a paleoaphebian succession showing evidence of atmospheric evolution. In: Young, G.M. (Ed.), Huronian Stratigraphy and Sedimentation. In: Geological Association of Canada Special Paper, vol. 12, pp. 31–47.
- Rudnick, R.L., Gao, S., 2003. The composition of the continental crust. In: Rudnick, R.L. (Ed.), The Crust. Treatise on Geochemistry. Elsevier–Pergamon, Oxford, pp. 1–64.
- Rye, R., Holland, H.D., 1998. Paleosols and the evolution of atmospheric oxygen: a critical review. *Am. J. Sci.* 298 (8), 621–672.
- Sahoo, S.K., Planavsky, N.J., Kendall, B., Wang, X., Shi, X., Scott, C., Anbar, A.D., Lyons, T.W., Jiang, G., 2012. Ocean oxygenation in the wake of the Marinoan glaciation. *Nature* 489 (7417), 546–549.
- Scott, C., Lyons, T.W., Bekker, A., Shen, Y., Poulton, S.W., Chu, X., 2008. Tracing the stepwise oxygenation of the Proterozoic ocean. *Nature* 452 (7186), 456–459.
- Sekine, Y., Tajika, E., Tada, R., Hirai, T., Goto, K.T., Kuwatani, T., Goto, K., Yamamoto, S., Tachibana, S., Isozaki, Y., Kirschvink, J.L., 2011. Manganese enrichment in the Gowganda Formation of the Huronian Supergroup: a highly oxidizing shallow-marine environment after the last Huronian glaciation. *Earth Planet. Sci. Lett.* 307 (1–2), 201–210.
- Siebert, C., Kramers, J.D., Meisel, T., Morel, P., Nagler, T.F., 2005. PGE, Re–Os, and Mo isotope systematics in Archean and early Proterozoic sedimentary systems as proxies for redox conditions of the early Earth. *Geochim. Cosmochim. Acta* 69 (7), 1787–1801.
- Starck, D., Papa, C.d., 2006. The northwestern Argentina Tarija Basin: stratigraphy, depositional systems, and controlling factors in a glaciated basin. *J. South Am. Earth Sci.* 22, 169–184.
- Sutcliffe, O.E., Dowdeswell, J.A., Whittington, R.J., Theron, J.N., Craig, J., 2000. Calibrating the Late Ordovician glaciation and mass extinction by the eccentricity cycles of Earth's orbit. *Geology* 28, 967–970.
- Taylor, S.R., McLennan, S.M., 1985. The Continental Crust: Its Composition and Evolution. Blackwell Scientific, Oxford. 312 pp.
- Visser, J.N.J., 1982. Upper Carboniferous glacial sedimentation in the Karoo Basin near Prieska, South Africa. *Palaeogeogr. Palaeoclimatol. Palaeoecol.* 38 (1–2), 63–92.
- Walker, J.C.G., Hays, P.B., Kasting, J.F., 1981. A negative feedback mechanism for the long-term stabilization of Earth's surface temperature. *J. Geophys. Res.* 86, 9776–9782.
- White, A.F., Bullen, T.D., Vivit, D.V., Schulz, M.S., Clow, D.W., 1999. The role of disseminated calcite in the chemical weathering of granitoid rocks. *Geochim. Cosmochim. Acta* 63 (13–14), 1939–1953.
- Wille, M., Kramers, J.D., Nägler, T.F., Beukes, N.J., Schröder, S., Meisel, T., Lacassie, J.P., Voegelin, A.R., 2007. Evidence for a gradual rise of oxygen between 2.6 and 2.5 Ga from Mo isotopes and Re–PGE signatures in shales. *Geochim. Cosmochim. Acta* 71 (10), 2417–2435.
- Wille, M., Nebel, O., Van Kranendonk, M.J., Schoenberg, R., Kleinhanss, I.C., Ellwood, M.J., 2013. Mo–Cr isotope evidence for a reducing Archean atmosphere in 3.46–2.76 Ga black shales from the Pilbara, Western Australia. *Chem. Geol.* 340, 68–76.
- Yang, W., Holland, H.D., 2003. The Hekpoort paleosol profile in Strata 1 at Gaborone, Botswana: soil formation during the Great Oxidation Event. *Am. J. Sci.* 303 (3), 187–220.
- Young, G.M., Nesbitt, H.W., 1982. Early Proterozoic climates and plate motions inferred from major element chemistry of lutites. *Nature* 299, 715–717.
- Young, G.M., Nesbitt, H.W., 1999. Paleoclimatology and provenance of the glaciogenic Gowganda Formation (Paleoproterozoic), Ontario, Canada: a chronostratigraphic approach. *Geol. Soc. Am. Bull.* 111 (2), 264–274.
- Young, G.M., von Brunn, V., Gold, D.J.C., Minter, W.E.L., 1998. Earth's oldest reported glaciation: physical and chemical evidence from the Archean Mozaan Group (~2.9 Ga) of South Africa. *J. Geol.* 106, 523–538.
- Young, G.M., Long, D.G.F., Fedo, C.M., Nesbitt, H.W., 2001. Paleoproterozoic Huronian basin: product of a Wilson cycle punctuated by glaciations and a meteorite impact. *Sediment. Geol.* 141–142, 233–254.
- Young, G.M., Minter, W.E.L., Theron, J.N., 2004. Geochemistry and palaeogeography of upper Ordovician glaciogenic sedimentary rocks in the Table Mountain Group, South Africa. *Palaeogeogr. Palaeoclimatol. Palaeoecol.* 214 (4), 323–345.
- Zhang, S., Jiang, G., Han, Y., 2008. The age of the Nantuo Formation and Nantuo glaciation in south China. *Terra Nova* 20, 289–294.
- Zhang, W., Hu, Z., Liu, Y., Chen, H., Gao, S., Gaschnig, R.M., 2012a. Total rock dissolution using ammonium bifluoride ( $\text{NH}_4\text{HF}_2$ ) in screw-top teflon vials: a new development in open-vessel digestion. *Anal. Chem.* 84 (24), 10686–10693.
- Zhang, W., et al., 2012b. Reassessment of  $\text{HF}/\text{HNO}_3$  decomposition capability in the high-pressure digestion of felsic rocks for multi-element determination by ICP-MS. *Geostand. Geoanal. Res.* 36 (3), 271–289.
- Zhou, C., Tucker, R., Xiao, S., Peng, Z., Yuan, X., Chen, Z., 2004. New constraints on the ages of Neoproterozoic glaciations in south China. *Geology* 32, 437–440.